

---

## Supplementary information

---

# Stability-limiting heterointerfaces of perovskite photovoltaics

---

In the format provided by the  
authors and unedited

Supplementary information for

**Stability-limiting heterointerfaces of perovskite photovoltaics**

Shaun Tan,<sup>1,9</sup> Tianyi Huang,<sup>1,9</sup> Ilhan Yavuz,<sup>2,9</sup> Rui Wang,<sup>1,3,\*</sup> Tae Woong Yoon,<sup>4</sup> Mingjie Xu,<sup>5</sup> Qiyu Xing,<sup>1</sup> Keonwoo Park,<sup>4</sup> Do-Kyoung Lee,<sup>6</sup> Chung-Hao Chen,<sup>1,7</sup> Ran Zheng,<sup>1</sup> Taegeun Yoon,<sup>4</sup> Yepin Zhao,<sup>1</sup> Hao-Cheng Wang,<sup>1,7</sup> Dong Meng,<sup>1</sup> Jingjing Xue,<sup>1</sup> Young Jae Song,<sup>4</sup> Xiaoqing Pan,<sup>5,8</sup> Nam-Gyu Park,<sup>6</sup> Jin-Wook Lee,<sup>4,\*</sup> and Yang Yang<sup>1,\*</sup>

<sup>1</sup>Department of Materials Science and Engineering and California NanoSystems Institute, University of California Los Angeles, Los Angeles, California 90095, USA.

<sup>2</sup>Department of Physics, Marmara University, 34722, Ziverbey, Istanbul, Turkey.

<sup>3</sup>School of Engineering, Westlake University and Institute of Advanced Technology, Westlake Institute for Advanced Study, Hangzhou 310024, China

<sup>4</sup>SKKU Advanced Institute of Nanotechnology (SAINT) and Department of Nanoengineering, Sungkyunkwan University, Suwon 16419, Republic of Korea.

<sup>5</sup>Irvine Materials Research Institute, University of California, Irvine, California 92697, USA.

<sup>6</sup>School of Chemical Engineering, Sungkyunkwan University, Suwon 16419, Republic of Korea.

<sup>7</sup>Department of Materials Science and Engineering, National Yang Ming Chiao Tung University, Hsinchu 30010, Taiwan.

<sup>8</sup>Department of Materials Science and Engineering and Department of Physics and Astronomy, University of California, Irvine, California 92697, USA.

<sup>9</sup>These authors contributed equally to this work.

**\*Corresponding authors:**

R. Wang, email: [wr2332317@ucla.edu](mailto:wr2332317@ucla.edu)

J.-W. Lee, email: [jw.lee@skku.edu](mailto:jw.lee@skku.edu)

Y. Yang, email: [yangy@ucla.edu](mailto:yangy@ucla.edu)

### **Supplementary Note 1: Further discussion on the heterointerface energy band diagrams**

In Extended Data Fig. 3, the perovskite bulk work function should also be affected by  $\Delta E_{\text{vac}}$ . This is because the less negative  $\Delta E_{\text{vac}}$  by replacing OAI treatment with OATsO treatment resultantly delocalizes the accumulated electrons in the potential well, which enhances the electron density and thus electron quasi-fermi level ( $E_{fn}$ ) work function of the perovskite bulk. Moreover, the change in bulk work function by surface treatment would also affect the band alignment and thus charge accumulation at the perovskite/SnO<sub>2</sub> heterointerface. Indeed, a slightly increased hole accumulation was observed for the OATsO-treated device (Fig. 1h, i). However, although the hole quasi-fermi level ( $E_{fp}$ ) for the OATsO-treated device slightly up-shifted, its increase is not as significant as  $E_{fn}$ . The overall effect on the quasi-fermi level splitting is consistent with the slight  $V_{\text{OC}}$  enhancement by replacing OAI treatment with OATsO treatment (Extended Data Fig. 5).

## **Supplementary Note 2: Derivation of the charge density distribution from KPFM**

The electric field distribution across the device cross section,  $E(z)$ , was calculated from the contact potential difference,  $V(z)$ , according to the equation:<sup>1</sup>

$$E(z) = -\frac{d}{dz} \left[ V(z) - \frac{\Phi_{\text{tip}}(z)}{e} \right] = -\frac{d}{dz} V(z)$$

where  $\Phi_{\text{tip}}(z)$  is the work function of the probe and  $e$  is the elementary charge.  $\frac{\Phi_{\text{tip}}(z)}{e}$  is constant. The charge density distribution in a device,  $\Delta\rho(z)$ , is then given by:<sup>1</sup>

$$\Delta\rho(z) = \epsilon_0 \epsilon_r \frac{d}{dz} E(z)$$

where  $\epsilon_0$  and  $\epsilon_r$  are the vacuum and relative permittivity, respectively. In accordance with the previous report,<sup>1</sup> the data were smoothed with the Savitzky–Golay processing by a second order polynomial regression and the same ratio of data points.

### **Supplementary Note 3: Further discussion on the low-dimensional phase formation**

Surface-sensitive GIXRD ( $\omega = 0.2^\circ$ , penetration depth  $< 60$  nm) revealed that only OAI and OABr treatments form 2D perovskites. OABF<sub>4</sub>, OATFA, and OATsO all did not form 2D perovskites (Supplementary Fig. 8), likely due to steric hindrance and the inability of asymmetrical counter-anions to be shaped into the ordered PbX<sub>6</sub><sup>4-</sup> octahedrons. We note that the observed negative  $\Delta E_{\text{vac}}$  and consequent charge obstruction/accumulation is separate and likely unrelated from 2D formation: (1) OABF<sub>4</sub> and OATFA do not form 2D perovskites, but their  $\Delta E_{\text{vac}}$  is still negative; (2) 2D perovskites are known to have low conductivity. Fundamentally, the low conductivity is because of the large organic cation (e.g. insulating alkyl group of alkylammonium), not the iodide or bromide anion. In this work, the organic cation is fixed as octylammonium; (3) Relatedly, halide orbitals contribute density of states to the perovskite band edge structure. Therefore, iodide or bromide *actually participate* in charge conduction; (4) It is actually possible for 2D perovskites to form a type II band alignment, which does not obstruct charge extraction. Therefore, 2D perovskite, by itself, cannot be used to explain the charge obstruction and accumulation observations; (5) Directly comparing OABF<sub>4</sub> and OATsO allows us to exclude any possible effects of 2D formation.

#### **Supplementary Note 4: Further discussion on the correlation between $\Delta E_{\text{vac}}$ , charge extraction, and device performance**

Based on Fig. 2e and Extended Data Fig. 5, we observed that the varying performance of the surface-passivated devices is mainly contributed by their differing *FFs*. A reduced *FF* is indicative of less efficient charge extraction. We postulate that this is related to  $\Delta E_{\text{vac}}$  as follows:

Firstly, the negative  $\Delta E_{\text{vac}}$  deepened the valence band offset (Supplementary Table 1) to worsen the energy level mismatch with spiro-MeOTAD (HOMO level: -5.2 eV). This sacrifices *FF* by reducing hole extraction into spiro-MeOTAD, which is observed as an increased charge extraction lifetime from the PL results (Fig. 2c, 2d). Similar phenomenon has been observed in published works that studied the charge extraction time after surface treatment by conventional alkylammonium salts paired with iodide or bromide as the counteranion.<sup>2,3</sup> Secondly, the negative  $\Delta E_{\text{vac}}$  created the heterointerface energy barrier seen from the KPFM device profiling, which also contributed to impede charge extraction to reduce *FF*.<sup>1,4,5</sup>  $\Delta E_{\text{vac}}$  progressively became less negative going from OAI treatment (-0.37 eV), to OABF<sub>4</sub> treatment (-0.22 eV), and to OATsO treatment (+0.07 eV). This minimizes the inefficient charge extraction trade-off, therefore maximizing the *FF* and PCE gains enabled by surface treatment. Consequently, the OATsO-treated devices have the best performance.

On the other hand, we observed that the *V<sub>OC</sub>* of the surface-passivated devices, while still different, are relatively less affected by a negative  $\Delta E_{\text{vac}}$  and inefficient charge extraction. Contrary to popular belief, from the perspective of the fundamental physics of solar cell operation, series resistance is actually not directly correlated with *V<sub>OC</sub>*.<sup>6,7</sup> Fundamentally, this is because at *V*=*V<sub>OC</sub>*, the current flow across a solar cell, in other words the current flow through the series resistance, is exactly equal to zero (*I*=0).<sup>7</sup> Published perovskite literature have also reported that the device *FF* can be more sensitive than *V<sub>OC</sub>* to inefficient charge extraction and potential energy barriers,<sup>4,5</sup> which supports our device results.

Finally, we further validated the generality of our observations and universality of our proposed strategy by applying it to a different, pure FAPbI<sub>3</sub> composition with DMSO replaced with NMP (fabrication details included in Methods). The results are presented in Extended Data Fig. 8 and Supplementary Table 3.

### **Supplementary Note 5: Contrasting the device degradation under MPP aging versus OC aging**

In general, we observed that all devices were less stable under OC stability test, compared to their corresponding degradation rate under MPP stability test. This is consistent with previous reports that studied PSC degradation behavior under different aging conditions.<sup>8</sup> That previous study showed that PSC degradation rate increases in the trend MPP aging < short-circuit aging < OC aging (i.e. PSCs have the worst stability under OC aging). Therefore, the OC stability test can be used to represent a conservative estimate of the PSC lifetime under maximum accelerated degradation, although we note that MPP aging is more truly reflective of real working PSCs.

Relatedly, a rapid “burn-in” decay stage is often observed during the first ~100 h of aging during PSC photostability tests.<sup>8–11</sup> Importantly, the “burn-in” decay has been shown to be more severe for OC aging, and less severe for MPP aging.<sup>8</sup> This is also consistent with our own observations (Fig. 2f). Although the “burn-in” decay is less noticeable under MPP stability tests, it nevertheless still exists, where the devices decayed at a more rapid rate in the first 100 h compared to the following ~400 h (Fig. 2f, Supplementary Table 4). Specifically, the OABF<sub>4</sub>-treated device performance decreased by -0.029 %/h in the first 100 h, compared to -0.014 %/h in the next 400 h. The OAI-treated device performance decreased by -0.064 %/h in the first 100 h, compared to -0.022 %/h for the next 400 h. Remarkably, the OATsO-treated devices displayed no obvious “burn-in” decay in both MPP aging and OC aging. General n-i-p devices are notoriously plagued by crippling initial “burn-in” decays,<sup>8,12</sup> so this improvement was already noteworthy.

## **Supplementary Note 6: Simulation of halide migration pathways by first principles**

The energy barriers of intra- and extra-lattice migration of halides were predicted by the associated reaction pathway energy profiles based on nudged elastic band (NEB) and constrained energy minimization methods in VASP. For intra-lattice migration, initial and final structures consisting of one vacancy in neighbouring halide sites in the 2x2x2 supercell were first generated and the structures were relaxed. We then performed a linear interpolation to generate the intermediate structures within defective initial and final structures. For extra-lattice migration, one selected halide atom on the relaxed  $\text{PbX}_2$  terminated surface was manually moved along the surface normal direction up to  $\sim 7\text{-}8\text{\AA}$  above the surface. The structures of this reaction pathway were also constructed by linear interpolation. For both intra- and extra-lattice migration energy profiles we used sufficiently large grid points. Energy barrier of halide migration are computed from the total energy difference between the initial (or final) state and saddle point. For the negatively charged environment, we found that energy corrections due to spurious charged defect-defect interactions in finite-size periodic cells in barrier calculations are around 0.02eV, i.e., they are negligibly small and may be excluded.

### **Supplementary Note 7: Half-device photostability tests**

For the half-device stability testing, half-devices of structure ITO/SnO<sub>2</sub>/perovskite, with or without surface treatment, were exposed to AM 1.5G illumination in a nitrogen glovebox (<100 ppm of O<sub>2</sub>/H<sub>2</sub>O). Periodically, a few half-devices were removed to deposit spiro-MeOTAD and electrode, to complete a full solar cell for *J-V* measurement. The remaining, unremoved half-devices were left untouched under AM 1.5G illumination. The recorded “time elapsed” in the figure plot refers only to the time exposed to illumination.

Although the half-devices are not real and complete PSCs, this experiment allows us to study the perovskite photostability by itself when ion migration (to penetrate and chemically corrode the charge-transport material/electrode) is excluded. Supplementary Fig. 14 plots the average over 4 half-devices for each condition. We found that the OAI-treated, OABF<sub>4</sub>-treated, and OATsO-treated half-devices all had approximately similar stability. Importantly, this result suggests that the photostability of the perovskite active layer, by itself, is not altered by the surface treatments. In other words, if the negative consequences induced by  $\Delta E_{\text{vac}}$  and ion migration are largely excluded, all surface-treated devices have comparable stability. In another perspective, this result also suggests that  $\Delta E_{\text{vac}}$  and its effect on ion migration are the dominant and primary factors that influence the degradation of complete, real working PSCs under illumination.

### **Supplementary Note 8: Possible mechanistic origins of $\Delta E_{\text{vac}}$**

Ligand-induced work function changes,  $\Delta W$ , is given by the relation:<sup>13–15</sup>

$$\Delta W = \frac{e}{\varepsilon_0 A} \Delta \mu = \frac{e}{\varepsilon_0 A} (\mu_{\text{dipole}} + \mu_{\text{charge}})$$

where  $e$  is the elementary charge,  $\varepsilon_0$  is the vacuum permittivity,  $A$  is the surface area, and  $\Delta \mu = \mu_{\text{dipole}} + \mu_{\text{charge}}$ .  $\mu_{\text{dipole}}$  and  $\mu_{\text{charge}}$  are two independent contributions,<sup>13–15</sup> where respectively,  $\mu_{\text{dipole}}$  is the ligand intrinsic dipole moment normal to the surface, while  $\mu_{\text{charge}}$  is related to a charge density displacement by interaction and bond formation of the ligand during chemisorption to the surface. The former is intensively reported in the perovskite community,<sup>16</sup> while the latter has been relatively less explored.  $\mu_{\text{charge}}$  is the primary mechanism by which low polarity (or non-polar) species cause a  $\Delta W$ . We first computed the respective dipole moments of various species in this work (Supplementary Fig. 15, 16). The negative  $\Delta W$  (i.e. more n-type) with increasing alkylammonium chain length is correlated with their successively increasing positive dipole moments. On the other hand, while both  $[\text{I}]^-$  and  $[\text{Br}]^-$  are non-polar, the experimentally measured  $\Delta W$  for the films treated with OAI or OABr were different (Fig. 1b), hinting of a contribution from  $\mu_{\text{charge}}$ . Additionally, the dipole moment of  $[\text{TsO}]^-$  has an opposite sign but only half that of  $[\text{OA}]^+$ , and thus the net dipole remains positive, which should have resulted in a negative  $\Delta W$ , and thus cannot fully explain the experimental observations. Therefore, the contribution of  $\mu_{\text{charge}}$  must be taken into consideration.

$\mu_{\text{charge}}$  is related to the charge density differential,  $\Delta \rho$ , as a function of position ( $x, y, z$ ) by:

$$\mu_{\text{charge}} \approx -e \iiint z \Delta \rho \, dx \, dy \, dz$$

The averaged charge density displacement as a function of  $z$ ,  $\Delta \bar{\rho}(z)$ , and charge displacement,  $\Delta q(z)$ , in terms of  $\Delta \bar{\rho}(z)$ , is given by:

$$\Delta \bar{\rho}(z) = \frac{1}{A} \iint \Delta \rho \, dx \, dy$$

$$\Delta q(z) = A \Delta \bar{\rho}(z) \Delta z$$

where  $\Delta \rho$  is calculated from:

$$\Delta \rho = \rho_{\text{complex}} - \rho_{\text{surface}} - \rho_{\text{ligand}}$$

Here,  $\rho_{complex}$ ,  $\rho_{surface}$  and  $\rho_{ligand}$  are the charge densities of the surface-ligand complex, free-standing surface, and free ligand, respectively. Subsequently, the charge displacement,  $\bar{q}$ , near the surface positioned at  $z_s$  is then calculated by:

$$\bar{q} = \frac{1}{\Delta z} \int_{z_s - \Delta z/2}^{z_s + \Delta z/2} \Delta q(z) dz$$

We computed the  $\Delta q(z)$  with the different ligands to explore the  $\mu_{charge}$  contribution (Fig. 4c-e). Strikingly,  $[TsO]^-$  induces a pronounced negative surface charge displacement,  $\bar{q}$ , of  $-0.022 e$ , three-fold larger in magnitude than the positive  $\bar{q}$  of  $[OA]^+$  of  $+0.006 e$ . Calculations with varying ligand surface density corroborate the trends (Supplementary Fig. 18). We did further calculations by introducing iodine vacancy ( $V_I$ ) or lead-iodine antisite ( $Pb_I$ ) defects to the surfaces of the slab models. Both defects have been reported to form readily on the perovskite surface.<sup>17,18</sup> We present our results in Supplementary Fig. 17 and Supplementary Table 7 below, which show that the charge displacement trends remained the same even on defected surfaces with  $V_I$  or  $Pb_I$ . Specifically,  $[OA]^+$  still induces a positive charge displacement ( $+\bar{q}$ ) even with either  $V_I$  or  $Pb_I$  present on the surface. On the other hand,  $[TsO]^-$  continues to induce a negative charge displacement ( $-\bar{q}$ ) that is larger in magnitude than the  $+\bar{q}$  of  $[OA]^+$ . Considering the results altogether, we therefore speculate that the contributions from both  $\mu_{charge}$  and  $\mu_{dipole}$  for  $[TsO]^-$  synergistically counterbalanced the otherwise negative work function change induced by  $[OA]^+$ . Consistent with this reasoning, for the other counter-anions, although the magnitudes of their negative  $\bar{q}$  are also larger than that of  $[OA]^+$  (Supplementary Fig. 18, Supplementary Table 6), their dipole moment contributions are however less than that of  $[TsO]^-$ , and therefore insufficient to negate the net negative  $\Delta W$ .

### **Supplementary Note 9: Pairing tosylate anion with alkylammoniums of different chain lengths**

We compared the performances of devices surface treated with either BATsO (BA: butylammonium), HATsO (HA: hexylammonium), OATsO (OA: octylammonium), and DATsO (DA: dodecylammonium). The alkyl chain length increases in the order: BA (4 carbons) < HA (6 carbons) < OA (8 carbons) < DA (12 carbons). In general, the device  $V_{OC}$  increases with longer alkyl chain length, whereas the  $FF$  decreases. As a result, the OATsO-treated devices showed the best performance, by achieving a balance between high  $V_{OC}$  and  $FF$  (Supplementary Fig. 19). We speculate that the  $V_{OC}$  trend is related to the cation dipole moments: the positive dipole moment increases with longer alkyl chain length (as we also calculated in Supplementary Fig. 15), which enhances the cation's interaction with traps to further reduce charge recombination at the heterointerface.<sup>16</sup> On the other hand, the  $FF$  seems to decrease with longer alkyl chain length, due to the insulating nature of the alkyl group to increase series resistance. A similar device performance trend with alkyl chain length was also observed for iodide-based salts in a previous work.<sup>3</sup>

### **Supplementary Note 10: Chemical structure and purity of the ammonium salts**

We used  $^1\text{H}$  NMR (400 MHz, DMSO-d<sub>6</sub>) to characterize the structure of our synthesized ammonium salt. We compared the chemical shift of the acid and amine reactants with the neutral salt product, shown in Supplementary Fig. 20 below. The reaction can be simply comprehended as a generic acid-base neutralization for organic species. The peaks of the reactants, p-Toluenesulfonic acid and octylamine (red and blue, respectively), remain almost unchanged in the salt product (black), except the proton on the sulfonyl group. Moreover, all peaks in the product shifted to lower-field regions compared to their corresponding original peaks. The chemical shift is particularly evident on proton e and f. Considering that proton e and f are closest to the ionic bond between the ammonium cation and tosylate anion, they are most susceptible to the inductive effect, and therefore exhibited the most evident variation of chemical shift. Since we mixed the reactants stoichiometrically, and the reaction is rapid and complete, very few reactants remained in the formed salt, as observed in the  $^1\text{H}$  NMR spectra. The purity of the product is thus very high.

## **Supplementary Tables**

**Supplementary Table 1.** Energy levels of the perovskite films. The work function (WF) and (ionization energy (IE) – WF) values are based on the UPS measurements. The vacuum level shift ( $\Delta E_{\text{vac}}$ ) and valence band maximum (VBM) values are calculated based on an aligned Fermi level.

	<b>WF (eV)</b>	<b>IE - WF (eV)</b>	<b><math>\Delta E_{\text{vac}}</math> (eV)</b>	<b>Aligned VBM (eV)</b>
Reference	4.74	0.69	-	-5.43
PEA <sup>+</sup> I <sup>-</sup>	4.52	0.73	-0.22	-5.47
BA <sup>+</sup> I <sup>-</sup>	4.45	0.79	-0.29	-5.53
OA <sup>+</sup> I <sup>-</sup>	4.37	0.86	-0.37	-5.60
DA <sup>+</sup> I <sup>-</sup>	3.89	0.96	-0.85	-5.70
OA <sup>+</sup> Br <sup>-</sup>	4.43	0.92	-0.31	-5.66
OA <sup>+</sup> BF <sub>4</sub> <sup>-</sup>	4.52	0.77	-0.22	-5.51
OA <sup>+</sup> TFA <sup>-</sup>	4.54	0.78	-0.20	-5.52
OA <sup>+</sup> TsO <sup>-</sup>	4.81	0.75	+0.07	-5.49

**Supplementary Table 2.** Time-resolved photoluminescence decay parameters of the glass/perovskite/spiro-MeOTAD films, fitted with a bi-exponential decay model.

	<b>A<sub>1</sub> (%)</b>	<b><math>\tau_1</math> (ns)</b>	<b>A<sub>2</sub> (%)</b>	<b><math>\tau_2</math> (ns)</b>	<b><math>\tau_{\text{ave}}</math> (ns)</b>
Reference	100.0	3.0	0.0	15.2	3.0
OAI-treated	94.5	7.5	5.5	19.8	8.1
OABF <sub>4</sub> -treated	99.1	4.7	0.9	17.4	4.8
OATsO-treated	99.9	3.5	0.1	17.7	3.5

**Supplementary Table 3.** Energy levels of the FAPbI<sub>3</sub> perovskite films. The work function (WF) and (ionization energy (IE) – WF) values are based on the UPS measurements. The vacuum level shift ( $\Delta E_{\text{vac}}$ ) and valence band maximum (VBM) values are calculated based on an aligned Fermi level.

	<b>WF (eV)</b>	<b>IE - WF (eV)</b>	<b><math>\Delta E_{\text{vac}}</math> (eV)</b>	<b>Aligned VBM (eV)</b>
FAPbI <sub>3</sub>	4.82	0.83	-	-5.65
OA <sup>+</sup> I <sup>-</sup>	4.48	1.02	-0.34	-5.84
OA <sup>+</sup> BF <sub>4</sub> <sup>-</sup>	4.60	0.94	-0.22	-5.76
OA <sup>+</sup> TsO <sup>-</sup>	4.87	0.89	+0.05	-5.71

**Supplementary Table 4.** Comparison of the device degradation at different time periods during the MPP stability test.

	PCE drop (%)		Degradation rate (%/h)	
	First 100 h	Next ~400 h	First 100 h	Next ~400 h
OAI-treated device	-6.4	-8.9	-0.064	-0.022
OABF <sub>4</sub> -treated device	-2.9	-5.6	-0.029	-0.014
OATsO-treated device	~0	~0	-	-

**Supplementary Table 5.** Activation energy for iodine or bromine migration in a neutral uncharged or negatively charged environment calculated from first-principles nudged elastic band (NEB) simulations.

	Neutral (eV)	Negative (eV)	Difference (%)
<b>Intra-lattice</b>			
I in FAPbI <sub>3</sub>	0.335	0.205	- 38.7
Br in FAPbBr <sub>3</sub>	0.634	0.448	- 29.4
<b>Extra-lattice</b>			
I in FAPbI <sub>3</sub>	3.30	2.86	- 13.3
Br in FAPbBr <sub>3</sub>	3.68	3.03	- 17.8

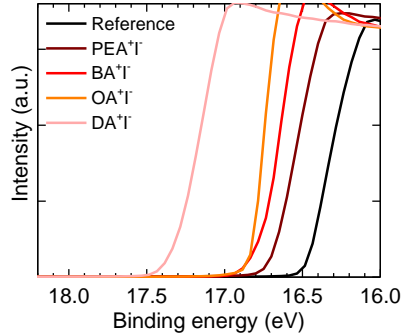
**Supplementary Table 6.** Surface charge displacement,  $\bar{q}$ , with different species attached to defect-free surfaces.

	$\bar{q}$ ( $\times 10^{-2} e$ )
[OA] <sup>+</sup>	+ 0.57
[I] <sup>-</sup>	- 1.33
[Br] <sup>-</sup>	- 1.40
[TFA] <sup>-</sup>	- 1.97
[TsO] <sup>-</sup>	- 2.19

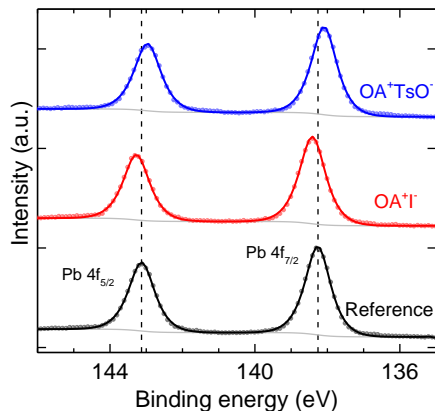
**Supplementary Table 7.** Surface charge displacement,  $\bar{q}$ , with different species attached to defected surfaces.  $V_I$  and  $Pb_I$  represent iodine vacancy and lead-iodine antisite defects, respectively, which may readily form on the perovskite surface due to their low formation energies.<sup>17,18</sup>

$\bar{q}$ ( $\times 10^{-2} e$ )	
<b><u>Surface with <math>V_I</math></u></b>	
[OA] <sup>+</sup>	+ 0.91
[TsO] <sup>-</sup>	- 1.76
<b><u>Surface with <math>Pb_I</math></u></b>	
[OA] <sup>+</sup>	+ 1.54
[TsO] <sup>-</sup>	- 2.33

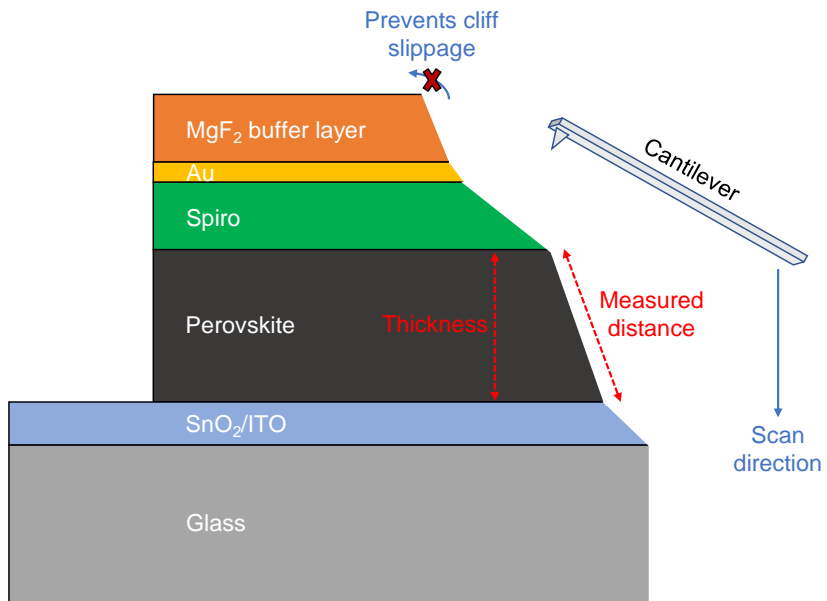
## **Supplementary Figures**



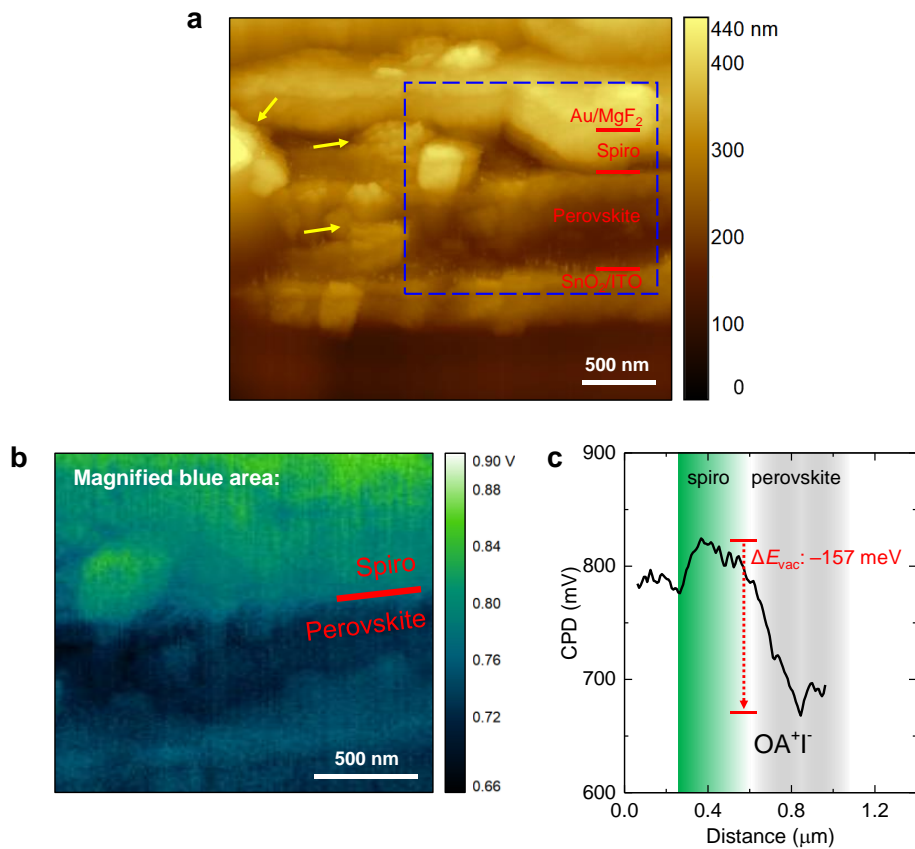
**Supplementary Figure 1. Work function change with ammonium iodide surface treatments.** UPS secondary electron cut-offs of perovskite films treated with various ammonium iodide salts. Labels are PEA: phenylethylammonium, BA: butylammonium, OA: octylammonium, DA: dodecylammonium.



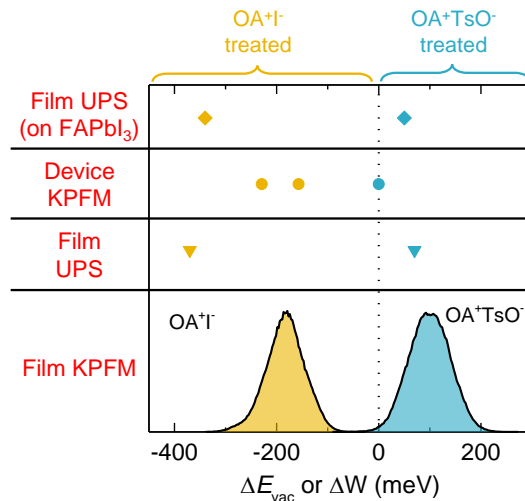
**Supplementary Figure 2. XPS characterization of the films.** High-resolution Pb 4f spectra of the films. Dashed vertical lines demarcate the peak positions for the Reference film. The Pb 4f peaks of the OAI-treated film shifted to a higher binding energy relative to the Reference film, consistent with the interaction of alkylammonium iodides with Pb.<sup>19</sup> For the OATsO-treated film, the shift to lower binding energy is also consistent with the interaction of the -SO<sub>3</sub><sup>-</sup> group of [TsO]<sup>-</sup> with Pb.<sup>20</sup>



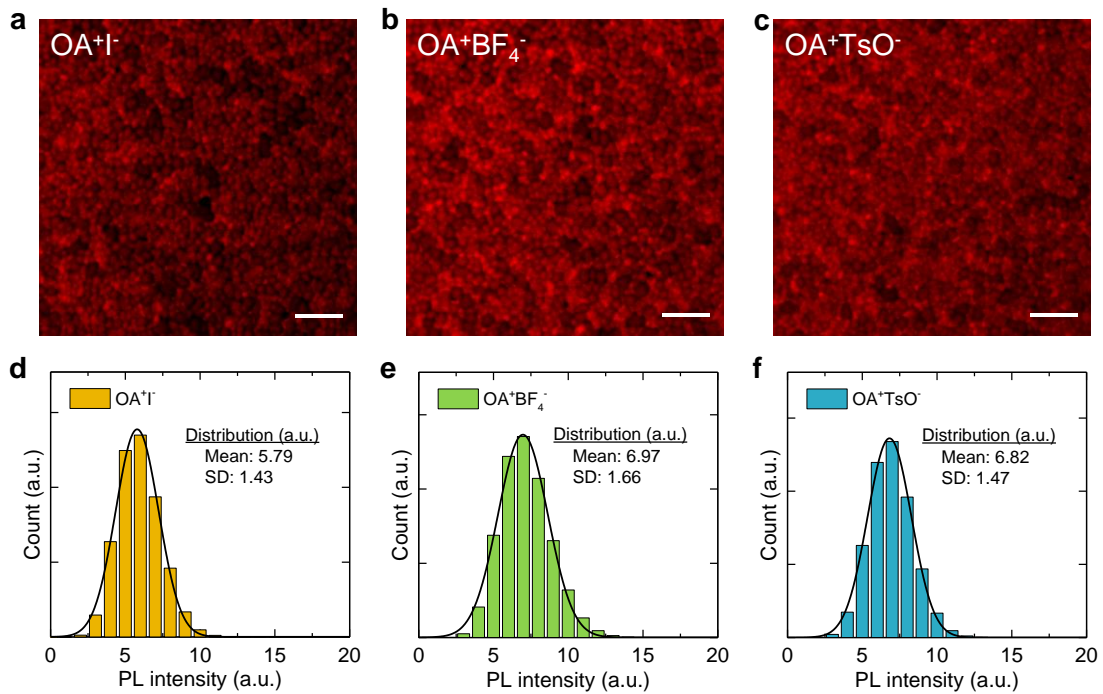
**Supplementary Figure 3. Cross-sectional KPFM schematic.** Schematic illustrating the KPFM measurement setup and planar device structure of ITO/SnO<sub>2</sub>/perovskite/spiro-MeOTAD/Au. The MgF<sub>2</sub> buffer layer prevents slippage of the cantilever tip at a “cliff”. Often, the device cross-sections are not parallel, due to the uncontrollable nature of the mechanical cleaving process. Therefore, the measured distance may not represent the layer thickness. Note that we purposely avoided using FIB or mechanical polishing for the KPFM samples, as such processing may modify the properties of the exposed cross-sectional surface.<sup>21</sup>



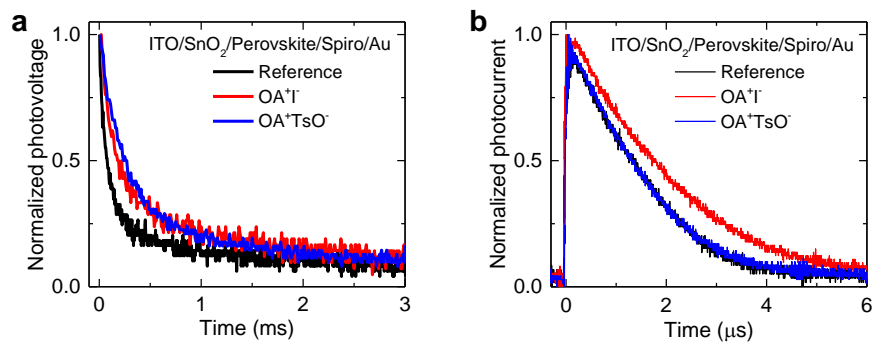
**Supplementary Figure 4. Cross-sectional KPFM profiling of another OAI-treated device.** **a**, AFM spatial mapping of an OAI-treated device. Yellow arrows in (a) indicate damaged regions due to the mechanical cleaving process. **b**, KPFM spatial mapping, and **c**, CPD profile of the OAI-treated device. The magnified KPFM image in (b) spatially corresponds to the blue square region in (a). All scale bars represent 500 nm. The  $\Delta E_{\text{vac}}$  value from the CPD profile matches those previously measured as shown in Supplementary Fig. 5.



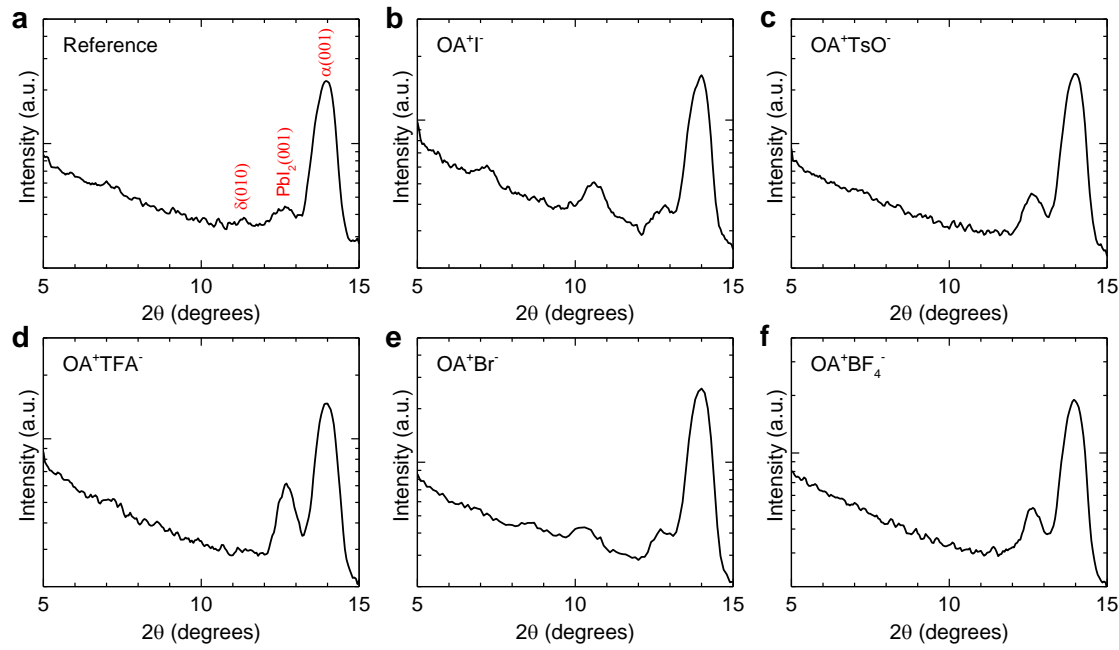
**Supplementary Figure 5. Different measurements of the vacuum level change.** Comparison of the  $\Delta E_{\text{vac}}$  or  $\Delta W$  of the perovskite devices or films measured from KPFM or UPS.



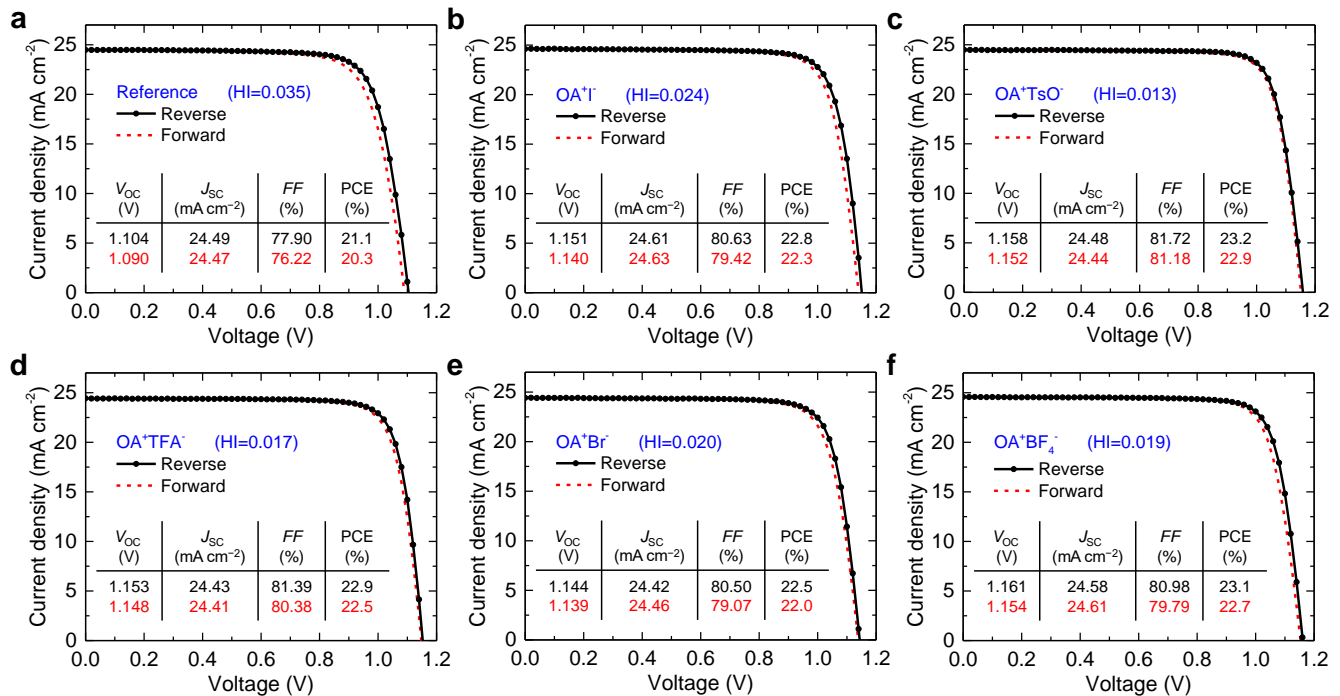
**Supplementary Figure 6. PL mapping of the passivated films.** Representative confocal PL maps of the **a**, OAI-treated, **b**, OABF<sub>4</sub>-treated, **c**, OATsO-treated perovskite films on glass. All scale bars represent 5  $\mu\text{m}$ . PL intensity distribution histograms of the **d**, OAI-treated, **e**, OABF<sub>4</sub>-treated, **f**, OATsO-treated perovskite films on glass. Insets include the fitted statistical parameters. SD: standard deviation.



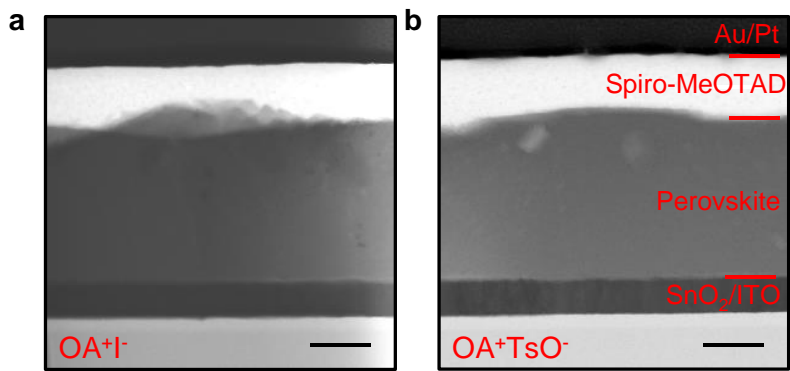
**Supplementary Figure 7. Photo-transient measurements of the complete devices.** Normalized **a**, transient photovoltage decay and **b**, transient photocurrent decay of the complete devices.



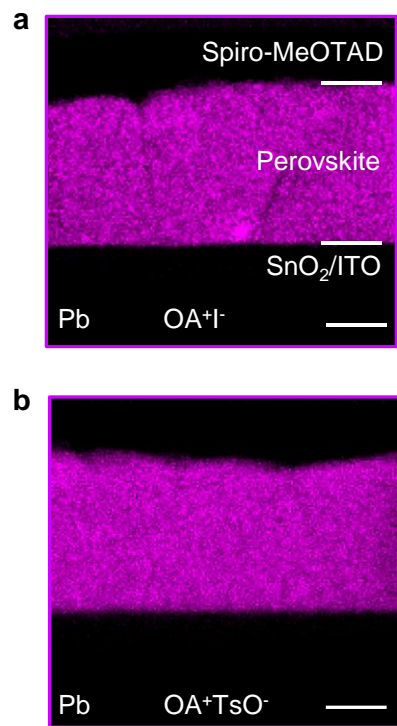
**Supplementary Figure 8. GIXRD characterization of the films.** Grazing incidence X-ray diffraction (GIXRD) of the **a**, Reference, **b**, OAI-treated, **c**, OATsO-treated, **d**, OATFA-treated, **e**, OABr-treated, and **f**, OABF<sub>4</sub>-treated perovskite films. Measurements were performed at an  $\omega = 0.2^\circ$ , with an estimated penetration depth of <60 nm.



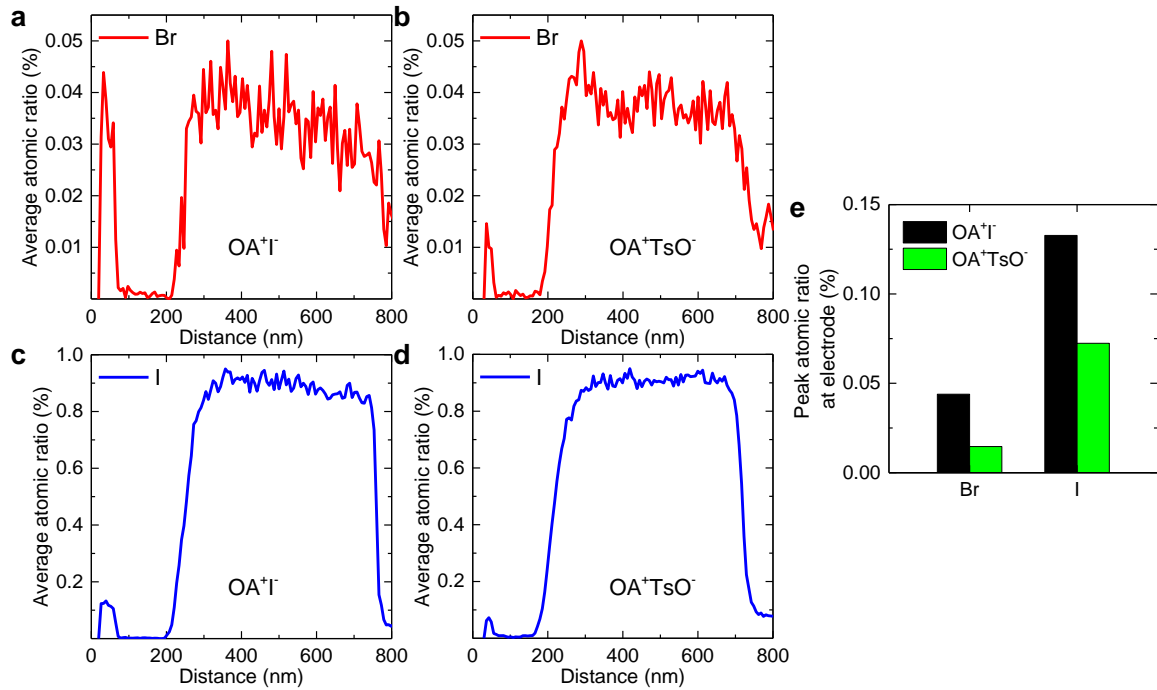
**Supplementary Figure 9. Device hysteresis behavior.** **a**, Current density-voltage curve of the **a**, Reference, **b**, OAI-treated, **c**, OATsO-treated, **d**, OATFA-treated, **e**, OABr-treated, and **f**, OABF<sub>4</sub>-treated devices, in reverse bias (black solid lines) and forward bias (red dashed lines). Insets include the measured photovoltaic parameters. We note that these devices did not have the MgF<sub>2</sub> anti-reflection coating. The hysteresis index (HI) is included in the insets.



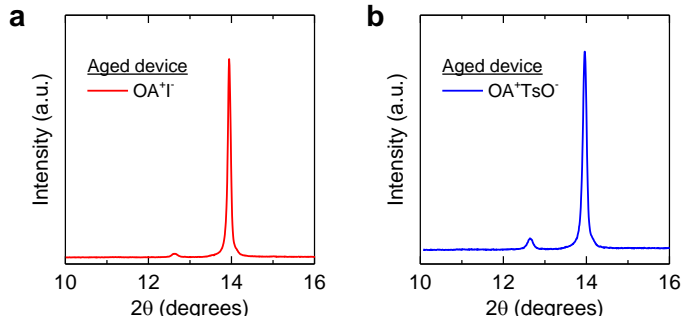
**Supplementary Figure 10. STEM images of the aged devices.** STEM bright field images of the aged **a**, OAI-treated and **b**, OATsO-treated device cross-sections. All scale bars represent 200 nm.



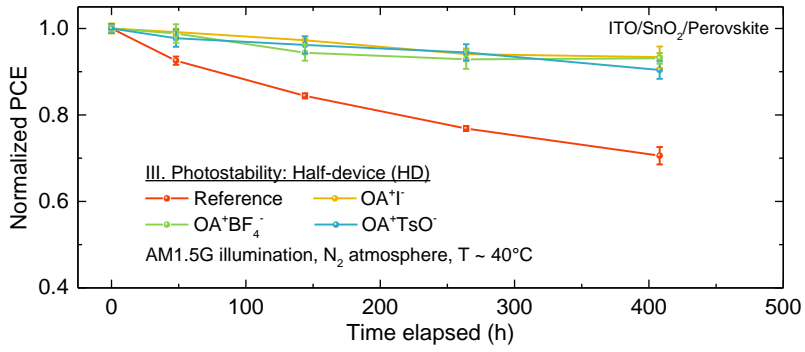
**Supplementary Figure 11. EDX analyses of the aged devices.** EDX elemental maps of lead for the **a**, OAI-treated and **b**, OATsO-treated device cross-sections. All scale bars represent 200 nm.



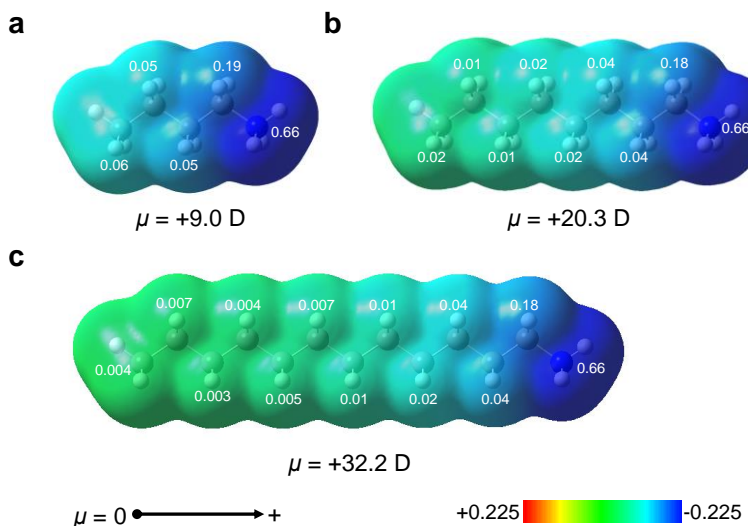
**Supplementary Figure 12. Halide distribution in the aged devices.** Average atomic ratio distributions across the **a**, OAI-treated and **b**, OATsO-treated device cross-sections, and iodine for the **c**, OAI-treated and **d**, OATsO-treated device cross-sections. **e**, Peak values extracted from (a)-(d) at the electrode region. The average atomic ratios were calculated by simply multiplying the normalized signal intensity with the nominal perovskite stoichiometry.



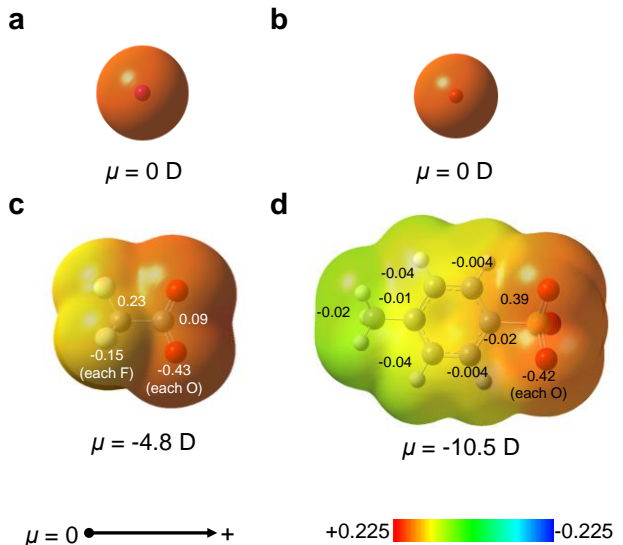
**Supplementary Figure 13. XRD analyses of the aged devices.** XRD diffraction patterns measured with an  $\omega$ - $2\theta$  setup of the aged **a**, OAI-treated and **b**, OATsO-treated devices. These were the same devices used for the STEM analyses, and were recovered after FIB milling. X-rays from the  $\omega$ - $2\theta$  diffraction setup were able to penetrate through the top electrode and spiro-MeOTAD layers to probe the active layer itself. Concurrently, given the large penetration depth of  $\omega$ - $2\theta$  XRD ( $>700$  nm), it is not sensitive to the ultrathin 2D interlayer, which is only detectable by the GIXRD measurements.



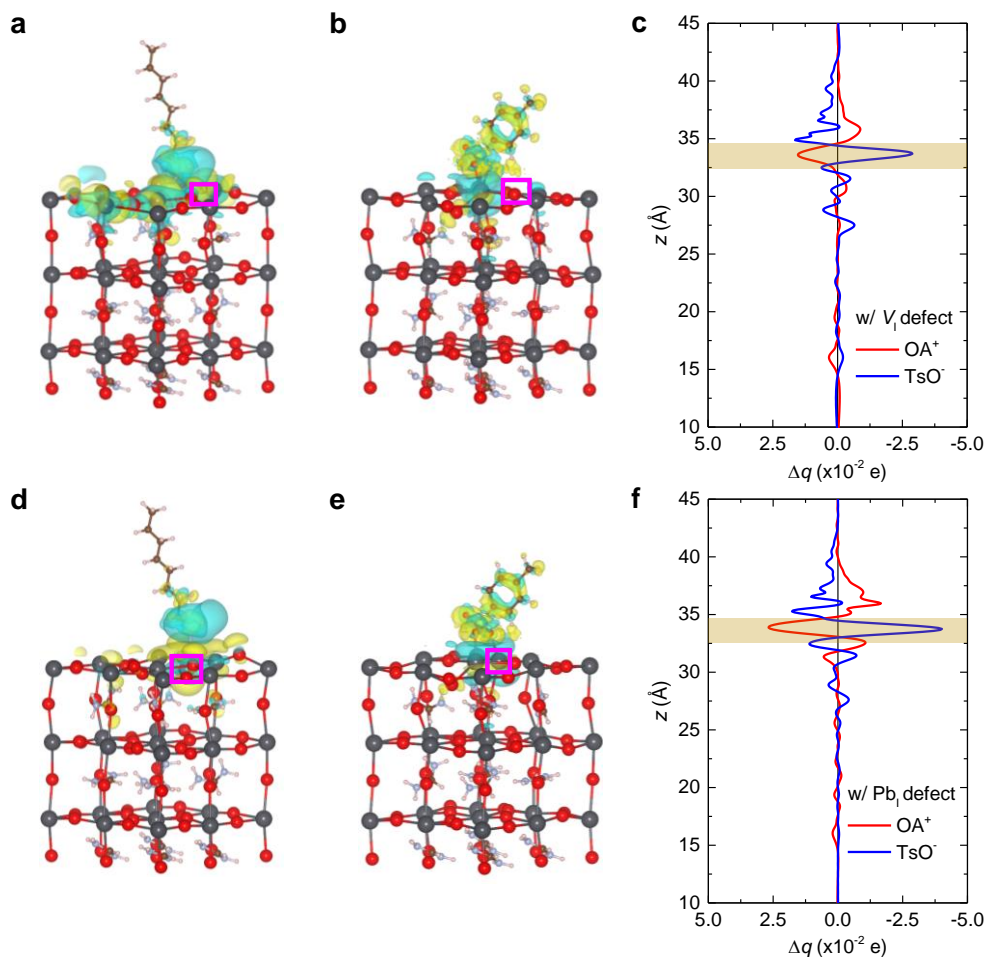
**Supplementary Figure 14. Half-device photostability test.** Stability evolution with time of half-devices aged under continuous illumination in a nitrogen atmosphere. The time elapsed refers only to the time under illumination. Error bars represent the standard deviation of four devices for each condition.



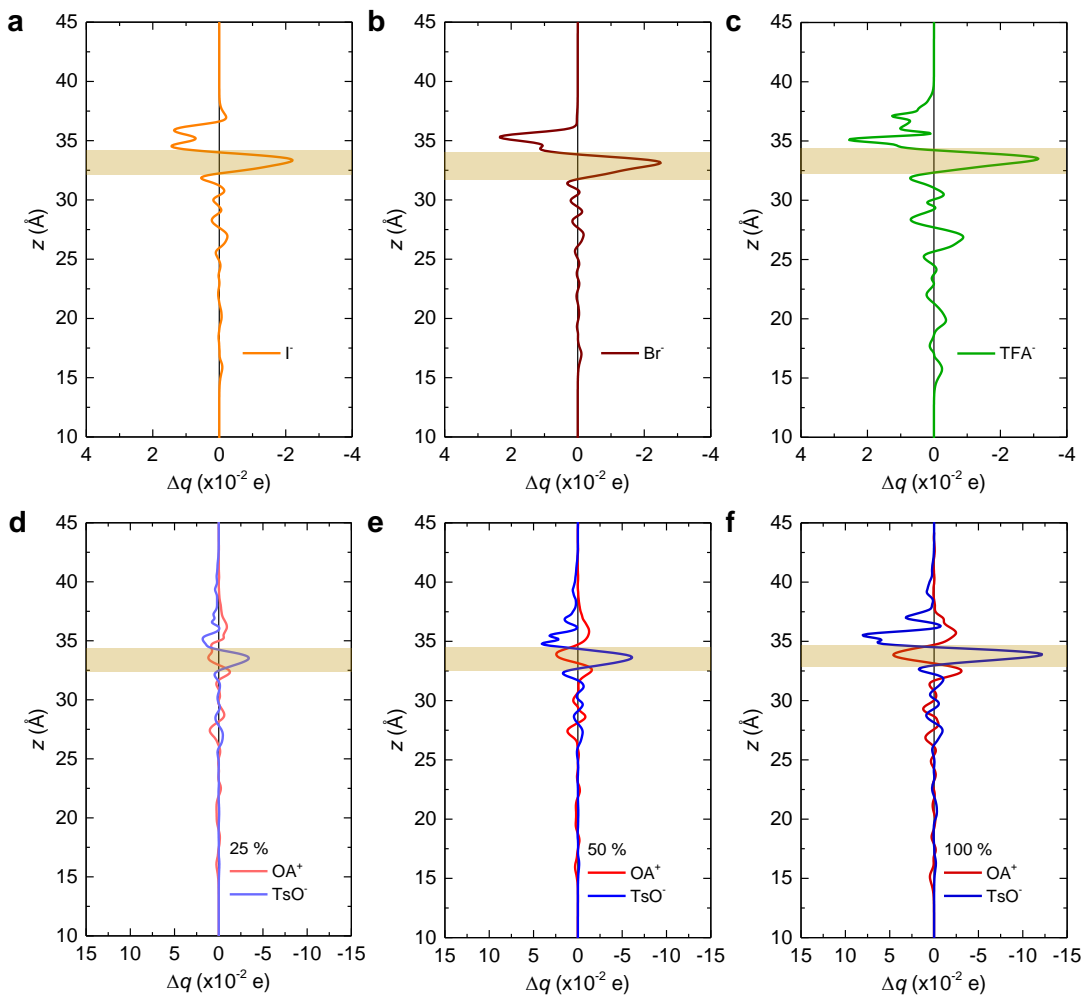
**Supplementary Figure 15. Electrostatic potentials of various cations.** Electrostatic potential maps of **a**,  $[\text{BA}]^+$ , **b**,  $[\text{OA}]^+$ , and **c**,  $[\text{DA}]^+$ . Included are their respective dipole moments ( $\mu$ ).



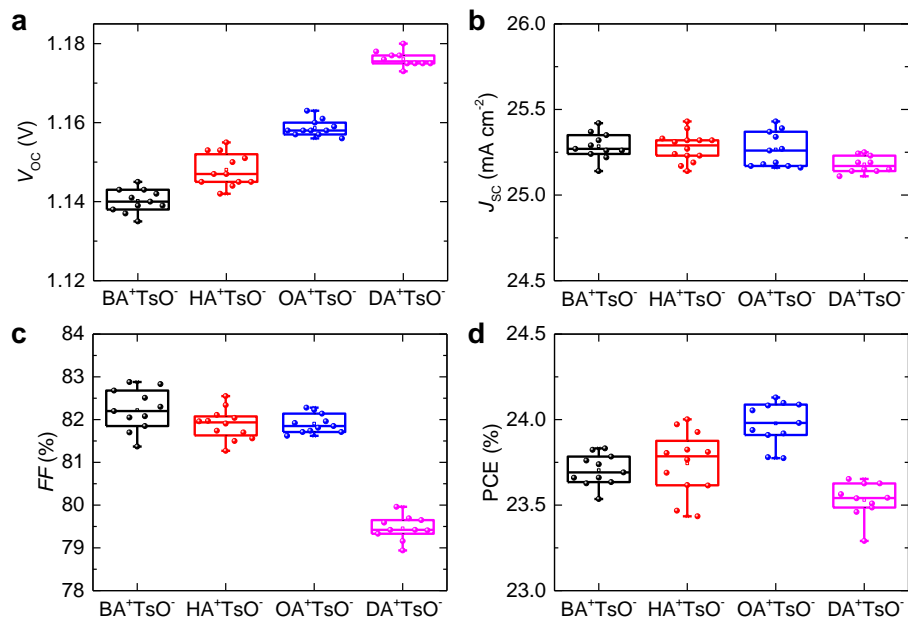
**Supplementary Figure 16. Electrostatic potentials of various anions.** Electrostatic potential maps of **a**,  $[I]^-$ , **b**,  $[Br]^-$ , **c**,  $[TFA]^-$ , and **d**,  $[TsO]^-$ . Included are their respective dipole moments ( $\mu$ ).



**Supplementary Figure 17. Surface states and charge displacement.** Charge displacement with surface iodine vacancy defect ( $V_I$ ) with **a**,  $[OA]^+$  or **b**,  $[TsO]^-$ , and **c**, corresponding charge displacement profiles. Charge displacement with surface lead-iodine antisite defect ( $Pb_I$ ) with **d**,  $[OA]^+$  or **e**,  $[TsO]^-$ , and **f**, corresponding charge displacement profiles. Blue and yellow volumes on the slab models correspond to electron-depleted or electron-enriched regions, respectively. The point defects are marked by pink squares.

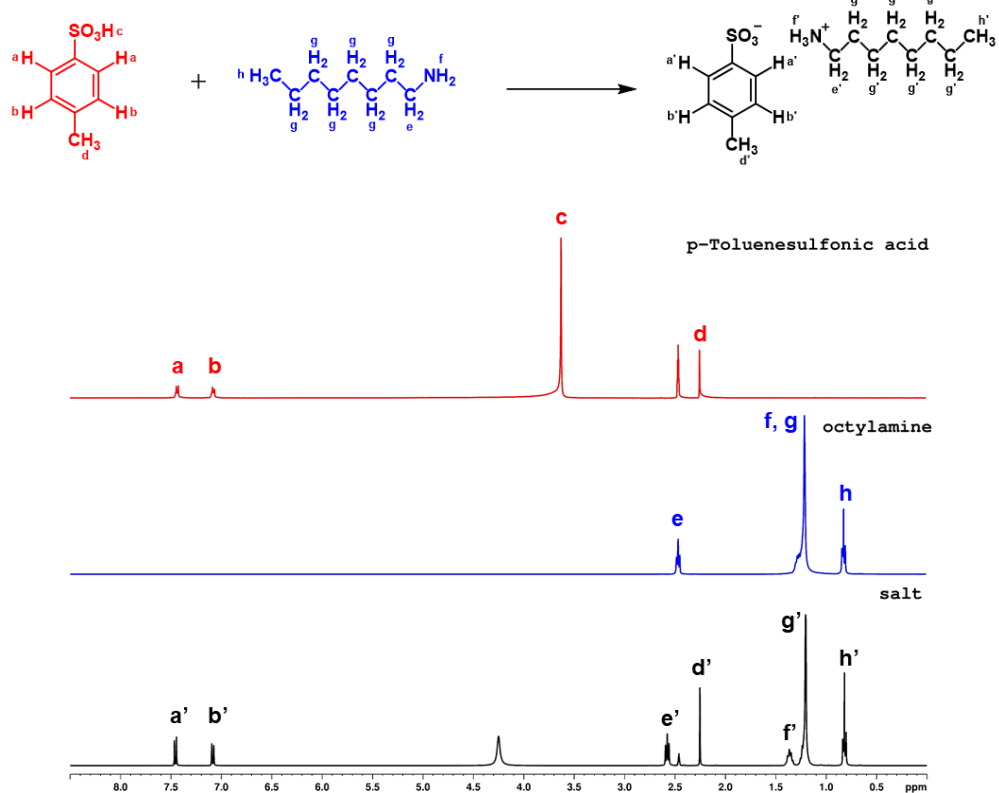


**Supplementary Figure 18. Charge displacement profiles with different anions and concentrations.** Charge displacement profiles on defect-free surfaces with **a**,  $[I^-]$ , **b**,  $[Br^-]$ , and **c**,  $[TFA^-]$ . Charge displacement profiles on defect-free surfaces with increasing  $[OA^+]$  or  $[TsO^-]$  surface concentration from **d**, 25 %, to **e**, 50 %, and to **f**, 100 %.



**Supplementary Figure 19. Device photovoltaic parameters with different tosylate-based salts.**

Box plots showing the distribution of the **a**,  $V_{OC}$ , **b**,  $J_{SC}$ , **c**,  $FF$ , and **d**, PCE of the devices. Center line: median, box limits: 25<sup>th</sup> and 75<sup>th</sup> percentile, whiskers: outliers.



**Supplementary Figure 20.** <sup>1</sup>H NMR spectra of p-Toluenesulfonic acid (red) and octylamine (blue) and OATsO salt (black) in DMSO-d<sub>6</sub>. The chemical structures and reaction scheme are shown above the spectra. All atoms are labelled for identifying their corresponding peaks in the spectra.

## **Supplementary References**

1. Bergmann, V. W. *et al.* Local Time-Dependent Charging in a Perovskite Solar Cell. *ACS Appl. Mater. Interfaces* **8**, 19402–19409 (2016).
2. Yoo, J. J. *et al.* An interface stabilized perovskite solar cell with high stabilized efficiency and low voltage loss. *Energy Environ. Sci.* **12**, 2192–2199 (2019).
3. Kim, H. *et al.* Optimal Interfacial Engineering with Different Length of Alkylammonium Halide for Efficient and Stable Perovskite Solar Cells. *Adv. Energy Mater.* **9**, 1902740 (2019).
4. Cai, M. *et al.* Control of Electrical Potential Distribution for High-Performance Perovskite Solar Cells. *Joule* **2**, 296–306 (2018).
5. Tsai, H. *et al.* Design principles for electronic charge transport in solution-processed vertically stacked 2D perovskite quantum wells. *Nat. Commun.* **9**, 2130 (2018).
6. Green, M. A. *Solar Cells: Operating Principles, Technology, and System Applications. Prentice Hall Series in Solid State Physical Electronics* (1981).
7. PVEducation. Solar Cell Operation: Series Resistance.  
<https://www.pveducation.org/pvcdrom/solar-cell-operation/series-resistance>. (accessed 01/20/2022).
8. Domanski, K., Alharbi, E. A., Hagfeldt, A., Grätzel, M. & Tress, W. Systematic investigation of the impact of operation conditions on the degradation behaviour of perovskite solar cells. *Nat. Energy* **3**, 61–67 (2018).
9. Tan, S. *et al.* Steric Impediment of Ion Migration Contributes to Improved Operational Stability of Perovskite Solar Cells. *Adv. Mater.* **32**, 1906995 (2020).
10. Wang, Z. *et al.* Efficient ambient-air-stable solar cells with 2D–3D heterostructured butylammonium-caesium-formamidinium lead halide perovskites. *Nat. Energy* **2**, 17135 (2017).
11. Bai, S. *et al.* Planar perovskite solar cells with long-term stability using ionic liquid additives. *Nature* **571**, 245–250 (2019).
12. Domanski, K. *et al.* Migration of cations induces reversible performance losses over day/night cycling in perovskite solar cells. *Energy Environ. Sci.* **10**, 604–613 (2017).
13. Brown, P. R. *et al.* Energy Level Modification in Lead Sulfide Quantum Dot Thin Films through Ligand Exchange. *ACS Nano* **8**, 5863–5872 (2014).
14. Heimel, G., Rissner, F. & Zojer, E. Modeling the Electronic Properties of  $\pi$ -Conjugated Self-Assembled Monolayers. *Adv. Mater.* **22**, 2494–2513 (2010).
15. de Boer, B., Hadipour, A., Mandoc, M. M., van Woudenberg, T. & Blom, P. W. M. Tuning of Metal Work Functions with Self-Assembled Monolayers. *Adv. Mater.* **17**, 621–625 (2005).
16. Lu, J. *et al.* Interfacial benzenethiol modification facilitates charge transfer and improves stability of cm-sized metal halide perovskite solar cells with up to 20% efficiency. *Energy Environ. Sci.* **11**, 1880–1889 (2018).
17. Wu, W.-Q. *et al.* Reducing Surface Halide Deficiency for Efficient and Stable Iodide-Based Perovskite Solar Cells. *J. Am. Chem. Soc.* **142**, 3989–3996 (2020).
18. Wang, R. *et al.* Constructive molecular configurations for surface-defect passivation of perovskite photovoltaics. *Science* **366**, 1509–1513 (2019).

19. Guo, Y. *et al.* Phenylalkylammonium passivation enables perovskite light emitting diodes with record high-radiance operational lifetime: the chain length matters. *Nat. Commun.* **12**, 644 (2021).
20. Liu, K. *et al.* Zwitterionic-Surfactant-Assisted Room-Temperature Coating of Efficient Perovskite Solar Cells. *Joule* **4**, 2404–2425 (2020).
21. Jiang, C.-S. *et al.* Carrier separation and transport in perovskite solar cells studied by nanometre-scale profiling of electrical potential. *Nat. Commun.* **6**, 8397 (2015).

# Stability-limiting heterointerfaces of perovskite photovoltaics

<https://doi.org/10.1038/s41586-022-04604-5>

Received: 4 May 2021

Accepted: 2 March 2022

Published online: 15 March 2022

 Check for updates

Shaun Tan<sup>1,11</sup>, Tianyi Huang<sup>1,11</sup>, Ilhan Yavuz<sup>2,11</sup>, Rui Wang<sup>1,3</sup>✉, Tae Woong Yoon<sup>4</sup>, Mingjie Xu<sup>5</sup>, Qiyu Xing<sup>1</sup>, Keonwoo Park<sup>4</sup>, Do-Kyoung Lee<sup>6</sup>, Chung-Hao Chen<sup>1,7</sup>, Ran Zheng<sup>1</sup>, Taegeun Yoon<sup>4</sup>, Yepin Zhao<sup>1</sup>, Hao-Cheng Wang<sup>1,7</sup>, Dong Meng<sup>1</sup>, Jingjing Xue<sup>1</sup>, Young Jae Song<sup>4,10</sup>, Xiaoqing Pan<sup>5,8</sup>, Nam-Gyu Park<sup>6,9</sup>, Jin-Wook Lee<sup>4,9</sup>✉ & Yang Yang<sup>1</sup>✉

Optoelectronic devices consist of heterointerfaces formed between dissimilar semiconducting materials. The relative energy-level alignment between contacting semiconductors determinately affects the heterointerface charge injection and extraction dynamics. For perovskite solar cells (PSCs), the heterointerface between the top perovskite surface and a charge-transporting material is often treated for defect passivation<sup>1–4</sup> to improve the PSC stability and performance. However, such surface treatments can also affect the heterointerface energetics<sup>1</sup>. Here we show that surface treatments may induce a negative work function shift (that is, more n-type), which activates halide migration to aggravate PSC instability. Therefore, despite the beneficial effects of surface passivation, this detrimental side effect limits the maximum stability improvement attainable for PSCs treated in this way. This trade-off between the beneficial and detrimental effects should guide further work on improving PSC stability via surface treatments.

Progress in compositional and crystal-growth engineering has made possible the fabrication of halide perovskite thin films with minimized bulk trap density, such that defects are predominantly located at the surface<sup>5,6</sup>. This has motivated the development of defect passivation treatments applied onto the top perovskite surface<sup>1–4</sup>. However, such treatments can also change the heterointerface energetics and thus the charge-carrier dynamics between the perovskite and the top charge-transporting material<sup>1</sup>. Here we study the consequences of the altered heterointerface energetics on carrier extraction, trap passivation, charge accumulation and ion migration. We show that a negative work function change ( $\Delta W$ ) accumulates charges in a potential well, which lowers the halide migration activation energy to limit the perovskite solar cell (PSC) stability. A negative  $\Delta W$  is equivalently described as a negative vacuum-level change ( $\Delta E_{\text{vac}}$ ) at a heterointerface, and hereafter,  $\Delta W$  and  $\Delta E_{\text{vac}}$  are used interchangeably.

## Perovskite surface and heterointerface dynamics

The genesis of this study began with our investigations on the surface energetics of perovskite films, based on a  $(\text{FAPbI}_3)_{0.95}(\text{MAPbBr}_3)_{0.05}$  composition (where FA is formamidinium and MA is methylammonium). Ultraviolet photoelectron spectroscopy (UPS) measurements showed that ubiquitously used ammonium-iodide-based surface treatments generally result in a negative  $\Delta W$  (Fig. 1a, Supplementary Fig. 1 and Supplementary Table 1), which successively

increases in magnitude with longer alkylammonium chain length. Given that a negative  $\Delta W$  is associated with a relatively more electron-enriched surface, we speculated initially that the negative  $\Delta W$  can be modulated by increasing the electron-withdrawing ability of the counteranion. Further UPS measurements (Fig. 1b) showed that substitution of iodide  $[\text{I}^-]$  with bromide  $[\text{Br}^-]$ , tetrafluoroborate  $[\text{BF}_4^-]$  or trifluoroacetate  $[\text{TFA}^-]$  progressively negated the negative  $\Delta W$  of octylammonium iodide (OAI) treatment towards that of the reference film, but only substitution with tosylate  $[\text{TsO}^-]$  fully neutralized the negative  $\Delta W$ . In particular, among the counteranions,  $[\text{TsO}^-]$  has the strongest electron-withdrawing character<sup>7</sup>, which also justifies its ubiquitous use as the leaving group in synthetic heterolytic fission chemistry. The interaction of  $[\text{TsO}^-]$  with the surface was further verified by X-ray photoelectron spectroscopy (XPS) analysis (Supplementary Fig. 2).

Kelvin probe force microscopy (KPFM) measurements were performed to verify the work function distributions (Fig. 1c–f). The mean work function of the OAI-treated film decreased to  $4.49 \pm 0.09$  eV, from  $4.67 \pm 0.08$  eV for the reference film, and in contrast to the  $4.77 \pm 0.11$  eV for the OATsO-treated film. From the topographical atomic force microscopy (AFM) maps, the surface morphology and root-mean-square roughness of the treated films were negligibly different (Fig. 1g), which was expected given the dilute (but common) solution concentration used for surface treatment. Further comparisons of the height-depth distributions and scanning electron microscopy

<sup>1</sup>Department of Materials Science and Engineering and California NanoSystems Institute, University of California Los Angeles, Los Angeles, CA, USA. <sup>2</sup>Department of Physics, Marmara University, Istanbul, Turkey. <sup>3</sup>School of Engineering, Westlake University and Institute of Advanced Technology, Westlake Institute for Advanced Study, Hangzhou, China. <sup>4</sup>SKKU Advanced Institute of Nanotechnology (SAINT) and Department of Nanoengineering, Sungkyunkwan University, Suwon, Republic of Korea. <sup>5</sup>Irvine Materials Research Institute, University of California Irvine, Irvine, CA, USA. <sup>6</sup>School of Chemical Engineering, Sungkyunkwan University, Suwon, Republic of Korea. <sup>7</sup>Department of Materials Science and Engineering, National Yang Ming Chiao Tung University, Hsinchu, Taiwan. <sup>8</sup>Department of Materials Science and Engineering and Department of Physics and Astronomy, University of California Irvine, Irvine, CA, USA. <sup>9</sup>SKKU Institute of Energy Science & Technology (SIES), Sungkyunkwan University, Suwon, Republic of Korea. <sup>10</sup>Center for Integrated Nanostructure Physics, Institute for Basic Science (IBS), Suwon, Republic of Korea. <sup>11</sup>These authors contributed equally: Shaun Tan, Tianyi Huang, Ilhan Yavuz. ✉e-mail: wangrui@westlake.edu.cn; jw.lee@skku.edu; yangy@ucla.edu

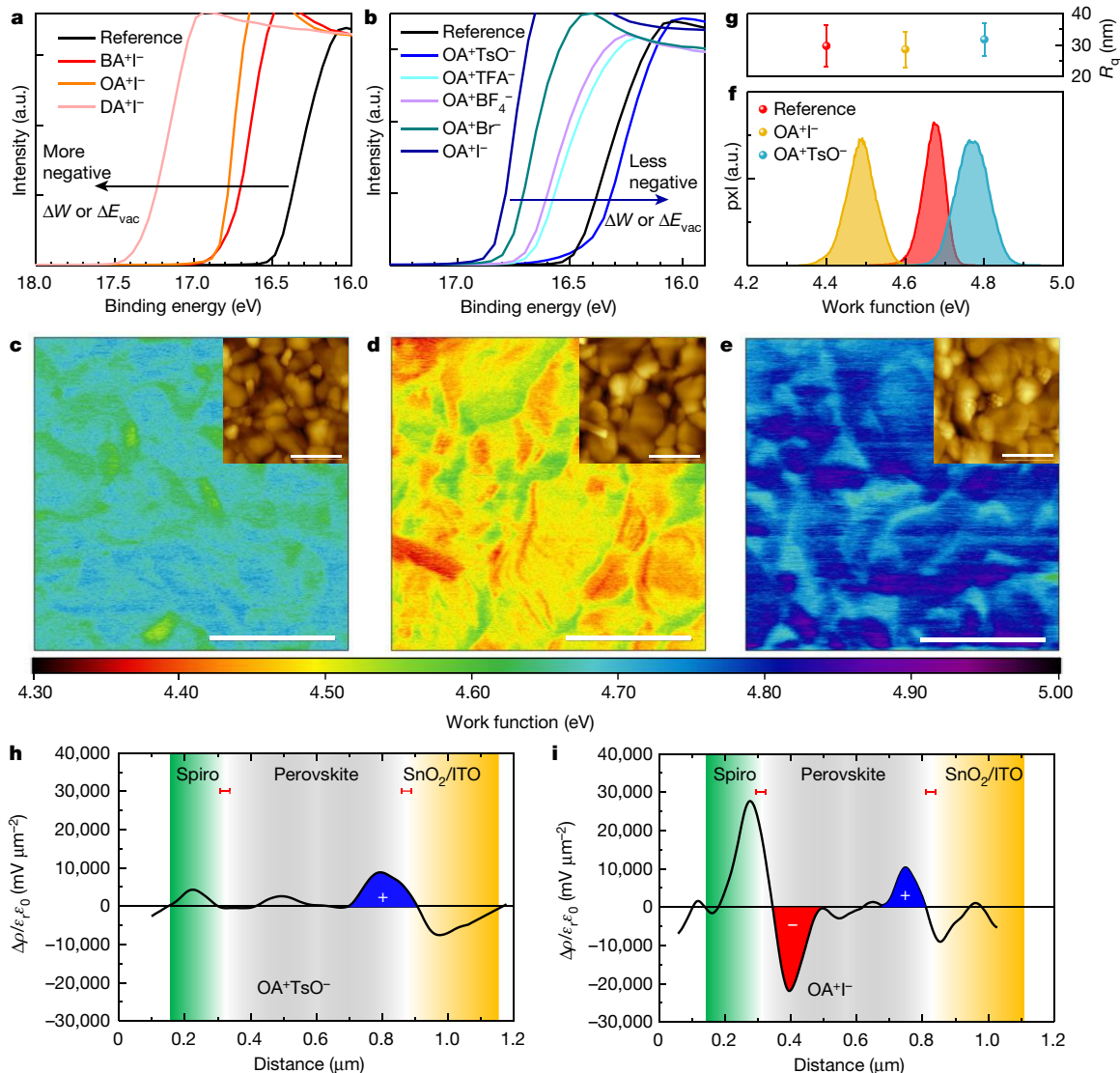


**Fig. 1 | Perovskite surface and heterointerface dynamics.** **a, b**, UPS secondary electron cut-offs of various surface-treated perovskite films. BA, butylammonium; DA, dodecylammonium; OA, octylammonium. **c–e**, KPFM surface potential maps of the reference (**c**), OAI-treated (**d**) and OATsO-treated (**e**) films. Insets, corresponding AFM topography images. Scale bars, 2  $\mu\text{m}$ . **f, g**, Work function distributions (**f**) and root-mean-square surface roughness ( $R_q$ ) (**g**) of the films measured by KPFM and AFM,

respectively. pxf, pixel. Error bars represent the standard deviation. **h, i**, Charge density distribution profiles of the complete OATsO-treated (**h**) and OAI-treated (**i**) device cross-sections measured by cross-sectional KPFM.  $\rho$ , charge density;  $\varepsilon_0$ , vacuum permittivity;  $\varepsilon_r$ , relative permittivity. The devices were illuminated under the OC condition. The red error bars demarcate the estimated spatial resolution of about 30 nm (refs. <sup>8,28</sup>).

(SEM) images also suggested that the surface uniformity is relatively similar for the treated films (Extended Data Figs. 1, 2).

## Consequences for charge-carrier dynamics

Band alignments constructed from the UPS results predict that a negative  $\Delta E_{\text{vac}}$  may create a potential well to trap charges at the heterointerface (Extended Data Fig. 3 and Supplementary Note 1). Cross-sectional KPFM measurements under illumination in the open-circuit (OC) condition were followed to investigate the real-time charge-carrier distributions in complete devices of planar-architecture indium tin oxide (ITO)/tin oxide (SnO<sub>2</sub>)/perovskite/2,2',7,7'-tetrakis[N,N-di(4-methoxyphenyl)amino]-9,9-spirobifluorene (spiro-MeOTAD)/gold (Au) (Extended Data Fig. 4, Supplementary Note 2 and Supplementary Figs. 3, 4). The measured device  $\Delta E_{\text{vac}}$  values at the perovskite/spiro-MeOTAD heterointerface are consistent with those obtained from the films (Supplementary Fig. 5). Charge carriers are unextractable in the OC condition (split quasi

Fermi level), and might accumulate at a contacting selective heterointerface of the opposite polarity<sup>8,9</sup>. This is observed as an accumulation of holes for both devices at the perovskite/SnO<sub>2</sub> heterointerface (Fig. 1h, i). In contrast, a pronounced electron accumulation exists at the perovskite/spiro-MeOTAD heterointerface for only the OAI-treated device. The electron accumulation is noted to be significantly more severe than the counterpart hole accumulation. In principle, the ideal photovoltaic device would have a homogeneous electric-field distribution with no charge accumulation across its heterojunctions<sup>10</sup>, which is seen for the OATsO-treated device at its perovskite/spiro-MeOTAD heterointerface. Both devices were relatively field-free (that is, flat potential) along the active layer, indicative of a high-quality perovskite bulk, suggesting that the different behaviours were a consequence of the surface treatments. The results are consistent with those predicted based on the band diagrams (Extended Data Fig. 3), where the non-negative  $\Delta E_{\text{vac}}$  of the OATsO-treated device avoided the potential well and charge accumulation.

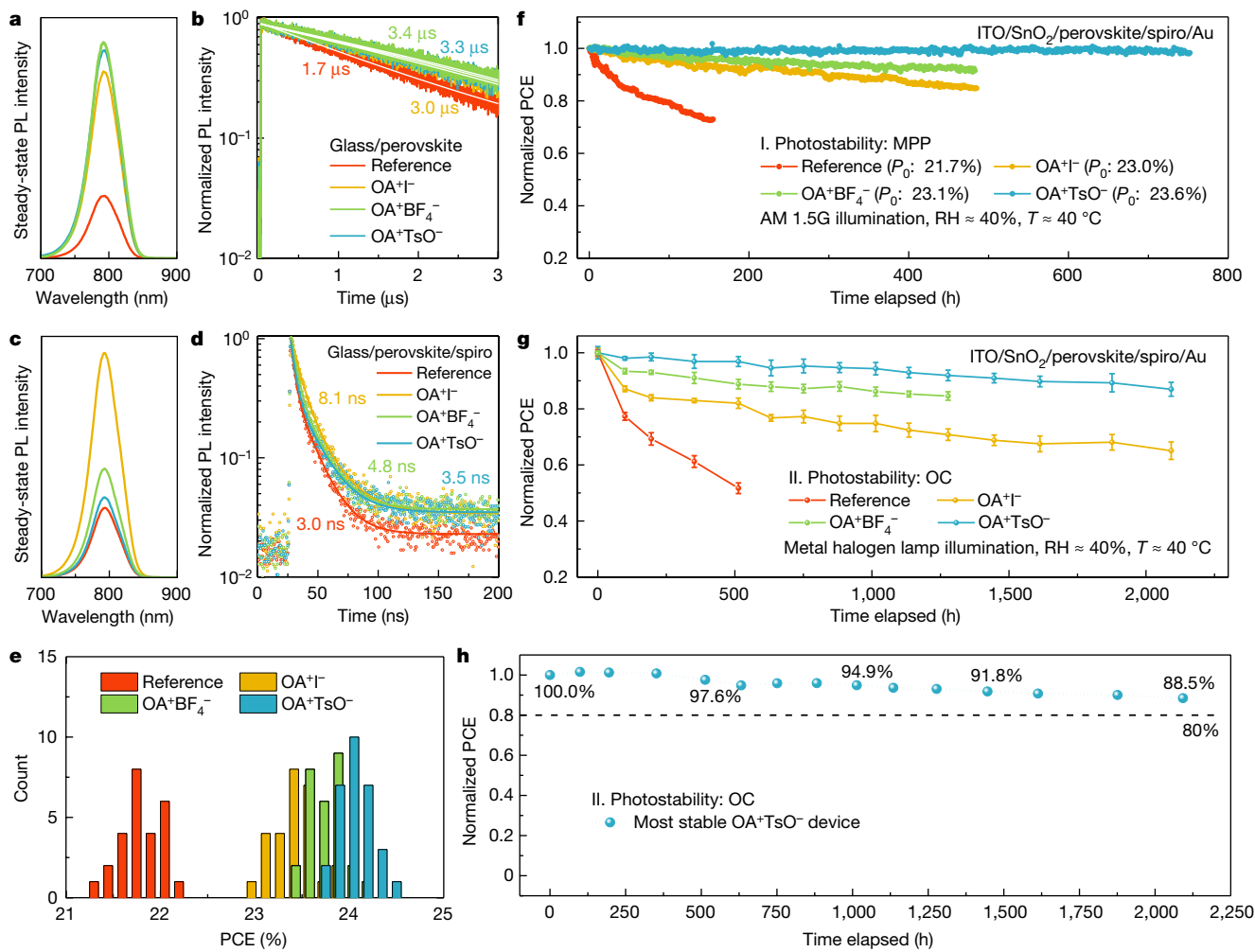


**Fig. 2 | Charge-carrier dynamics, performance and photostability.** **a, b.** Steady-state (**a**) and time-resolved (**b**) PL spectra of the glass/perovskite films. **c, d.** Steady-state (**c**) and time-resolved (**d**) PL spectra of the glass/perovskite/spiro-MeOTAD films. Included are the extracted lifetimes fitted with a mono-exponential decay function for **b** and a bi-exponential decay function for **d**. **e.** The PCE distributions of the devices. **f.** Photostability evolution with time of encapsulated devices aged under continuous

illumination at the MPP.  $P_0$  denotes the initial PCE. **g.** Photostability evolution with time of the encapsulated devices aged under continuous illumination in the OC condition. Error bars represent the standard deviation of four devices for each condition. **h.** Photostability PCE evolution of the most stable OATsO-treated device aged under the OC condition. Included are the PCE retentions in approximately 500-h intervals.

Photoluminescence (PL) spectroscopy indicated an effective suppression of charge-trapping defect states in the surface-treated films, as evidenced by their enhanced PL intensities and carrier lifetimes with a glass/perovskite architecture (Fig. 2a, b). The defect passivation efficacies of the surface-treated films are noted to be relatively comparable. Comparing their PL intensity distributions indicates again that the surface uniformity is similar between the films (Supplementary Fig. 6). Despite the beneficial passivation effects, charge extraction into spiro-MeOTAD is sacrificially impeded in all surface-treated films (Fig. 2c, d and Supplementary Table 2), but to different extents, with the trend correlated with the magnitude of  $\Delta E_{\text{vac}}$ . Compared with the reference/spiro-MeOTAD film, the average carrier lifetime ( $\tau_{\text{ave}}$ ) more than doubled to 8.1 ns (from 3.0 ns) for the OA<sup>+</sup>-treated film and the steady-state PL intensity was 223% higher. In contrast, OATsO treatment simultaneously suppressed the trap states whereas charge extraction was barely impeded, avoiding the trade-off seen for the OABF<sub>4</sub> and the OA<sup>+</sup> treatments. Further phototransient measurements on complete devices complement the film PL results (Supplementary Fig. 7). We postulate that the charge obstruction and accumulation cannot be explained by the surface two-dimensional phase, as the insulating large organic cation (OA<sup>+</sup>) is kept unchanged (Supplementary Note 3 and Supplementary Fig. 8).

## Device performance and hysteresis behaviour

For the surface-treated devices, the power conversion efficiency (PCE) shows the trend OATsO-treated devices > OABF<sub>4</sub>-treated devices > OA<sup>+</sup>-treated devices, owing primarily to an increasing fill factor (FF) (Fig. 2e and Extended Data Fig. 5). The device open-circuit voltages ( $V_{\text{oc}}$ ) are marginally different, reflective of the comparable PL results of the glass/perovskite films. The best OATsO-treated device reached a PCE of 24.41% (Extended Data Fig. 6). We further verified the performance of encapsulated devices at an independent third-party laboratory, noting that the performance slightly decreased after the encapsulation procedure (Extended Data Fig. 7). Contrasting the surface-treated devices, the PCE trend can be explained as follows (further discussion in Supplementary Note 4). First, a more negative  $\Delta E_{\text{vac}}$  deepened the valence band offset with spiro-MeOTAD, which increased the hole extraction resistance to sacrifice the FF. In addition, the heterointerface barrier observed from the KPFM profiling may also contribute to impede charge extraction<sup>9,11</sup>. Regardless, a negative  $\Delta E_{\text{vac}}$  remains the cause that gave rise to both effects. Separate investigations of a FAPbI<sub>3</sub> composition further verified our observations (Extended Data Fig. 8 and Supplementary Table 3).

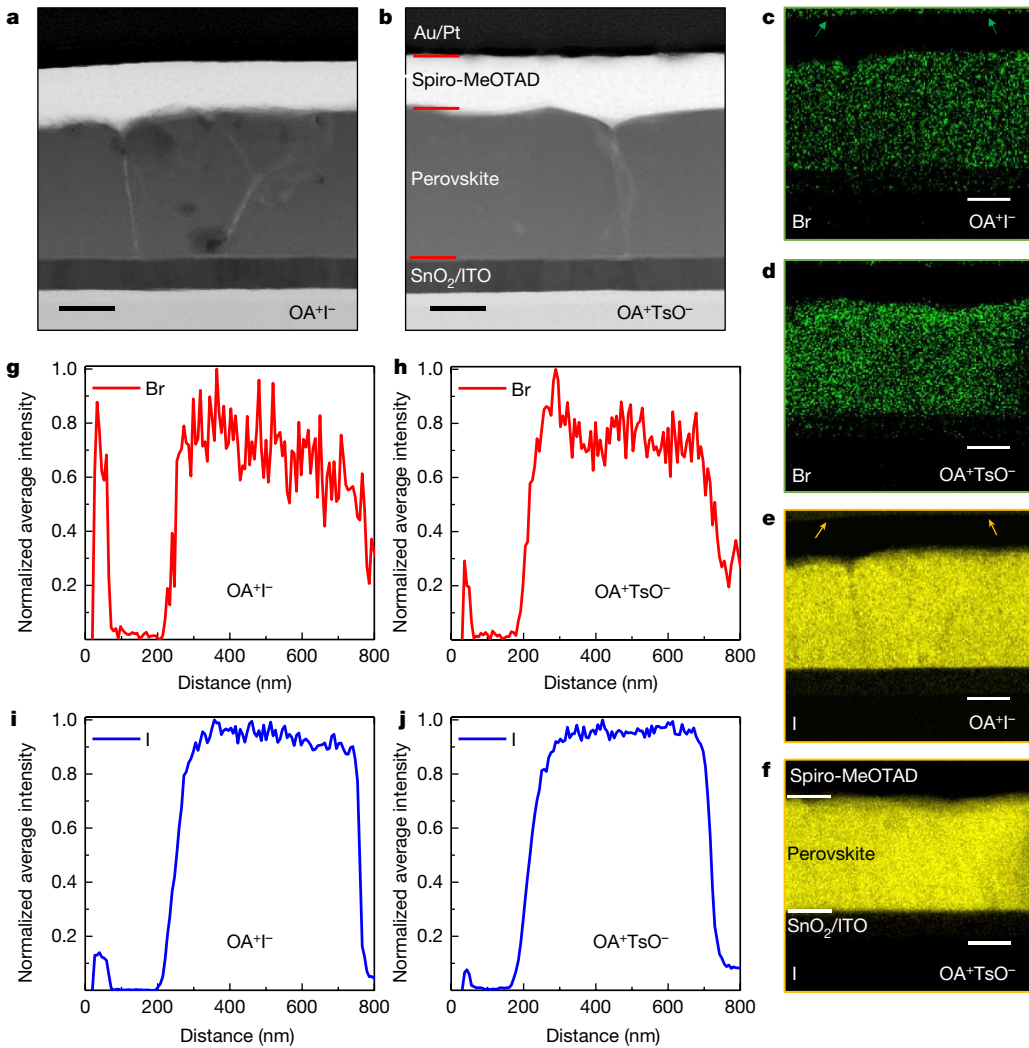


**Fig. 3 | STEM and EDX analyses of the aged devices.** **a, b**, STEM bright-field images of the aged OAI-treated (**a**) and OATsO-treated (**b**) device cross-sections. The OAI-treated device is seen to have a rougher heterointerface contacting spiro-MeOTAD. **c–f**, EDX elemental maps of

bromine (**c, d**) and iodine (**e, f**) for the OAI-treated (**c, e**) and OATsO-treated (**d, f**) device cross-sections. All scale bars in the STEM and EDX images represent 200 nm. **g–j**, Elemental distributions of bromine (**g, h**) and iodine (**i, j**) for the OAI-treated (**g, i**) and OATsO-treated (**h, j**) devices.

Comparing the surface-treated devices, the hysteresis behaviour generally improved as the negative  $\Delta E_{\text{vac}}$  decreased in magnitude (Supplementary Fig. 9). This provided the first hint at a correlation between  $\Delta E_{\text{vac}}$  and ion migration, given that ion migration is responsible for PSC hysteresis<sup>12,13</sup>. In contrast, the reference devices showed the lowest performance and worst hysteresis, owing to the abundant, unpassivated heterointerface traps. Overall, the device performance results provide evidence for the sacrificial trade-off of a negative  $\Delta E_{\text{vac}}$  to limit PSC performance.

### Device stability under continuous illumination

We assessed the photostability of encapsulated devices under continuous illumination without an ultraviolet filter. All devices were aged in an ambient atmosphere at about 40 °C. We preserved the original device architecture with spiro-MeOTAD as the hole-transporting material, without applying further modifications (for example, copper phthalocyanine (CuPC) or poly(triarylamine) (PTAA) were not used). Under maximum power point (MPP) testing (Fig. 2f), the OATsO-treated device sustained its performance with negligible degradation after about 800 h. The OABF<sub>4</sub>-treated device was also relatively stable, retaining 91.5% of its performance after about 500 h. Among the surface-treated

devices, the OAI-treated device degraded the most rapidly to 84.8% of its performance after about 500 h.

Contrasting the device degradation under MPP testing versus OC condition testing, all devices were generally less stable under OC condition testing (Fig. 2g, Extended Data Fig. 9 and Supplementary Note 5). However, the device degradation trends are identical, and correlated with the magnitude of  $\Delta E_{\text{vac}}$ . In particular, the OABF<sub>4</sub>-treated devices with an intermediate negative  $\Delta E_{\text{vac}}$  showed stability between that of the OAI-treated and the OATsO-treated devices. Near the approximate halfway point of 1,014 h, the devices retained 94.3% (OATsO treated), 86.2% (OABF<sub>4</sub> treated) and 74.8% (OAI treated) of their average PCEs. Ending after 2,092 h, the OATsO-treated devices retained 87.0% of their initial PCE on average. In contrast, the average PCE (65.1% of initial) of the OAI-treated devices decreased dramatically over the 2,092-h aging duration. The most stable OATsO-treated device (Fig. 2h) retained 94.9% and 88.5% of its initial PCE after 1,014 h and 2,092 h, respectively.

Analysing the degradation trends, we postulated that the potential well and charge accumulation may have accelerated ion migration, considering that the KPFM profiling was also performed under illumination in the OC condition. In particular, the more rapid ‘burn-in’ decay of the OAI-treated and the OABF<sub>4</sub>-treated devices, observed in both the MPP (Supplementary Table 4) and the OC tests, strongly hints that ion

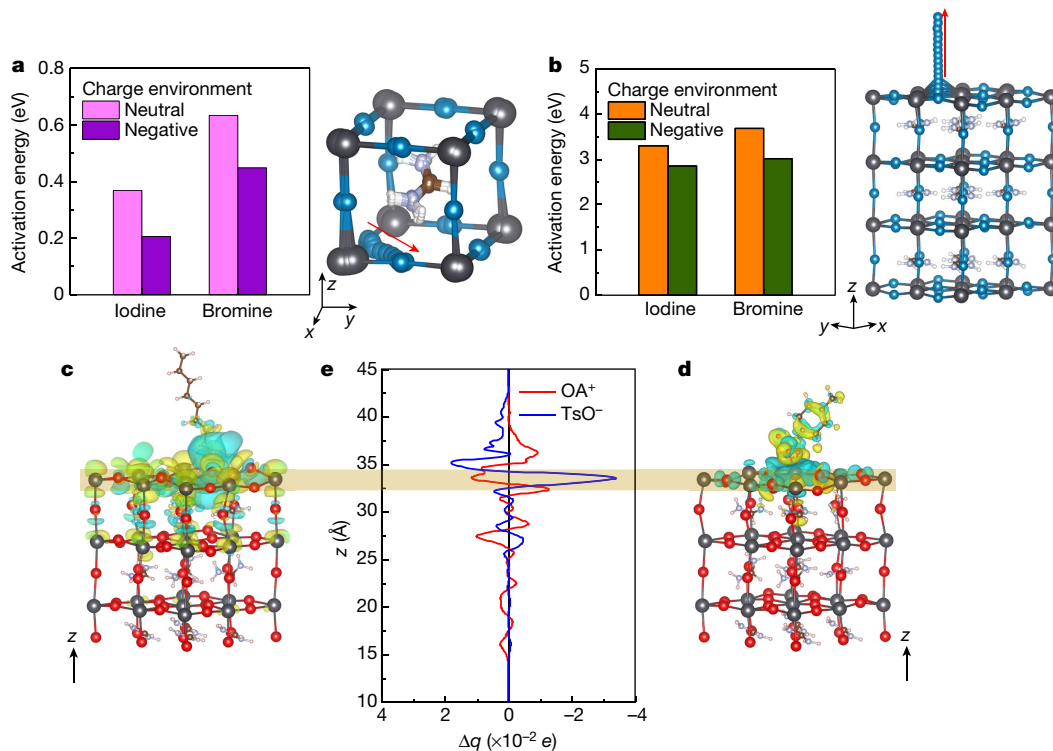


**Fig. 4 | Physical origins of the experimental observations.** **a, b**, Activation energy for the intra-lattice (**a**) and extra-lattice (**b**) migrations of iodine or bromine calculated using first-principles nudged-elastic-band simulations. The forward migration pathways are indicated by the red arrows in the example simulated supercells. **c–e**, Charge displacement with  $[OA^+]$  (**c**) or  $[TsO^-]$  (**d**) on the surface, superimposed on the defect-free slab models, and corresponding

charge displacement profiles (**e**). The blue and yellow volumes on the slab models correspond to electron-depleted or electron-enriched regions, respectively. The beige horizontal band spatially corresponds **c** and **d** with **e**. Black, Pb atoms; red, I atoms; blue, Br atoms; brown, C atoms; light blue, N atoms; white, H atoms.

migration has been aggravated by a negative  $\Delta E_{vac}$ , given that transient ion migration underlies the ‘burn-in’ regime<sup>12,14,15</sup>. The altered ion migration energetics was also hinted by the device hysteresis behaviour. Moreover, the two-dimensional interlayer of the conventional OAI treatment probably contributed to impeding ion migration<sup>16</sup>, yet the OABF<sub>4</sub>-treated and the OATsO-treated devices still had superior photostability, indicating that the ion migration energetics have been dominantly affected.

### Analyses of the degraded devices

To directly investigate the extent of ion migration, on completion of the OC stability testing, the original OAI-treated and OATsO-treated devices (after 2,092 h illumination) were sent for scanning transmission electron microscopy (STEM) analysis. The encapsulation cover glasses were detached immediately before focused ion beam (FIB) milling to extract sample cross-sections. STEM bright-field images of the planar device stacks revealed that the micrometre-scale grain sizes were still visibly intact even after the extended aging (Fig. 3a, b and Supplementary Fig. 10). The first notable difference between the two samples can be seen at the perovskite/spiro-MeOTAD heterointerface. The OAI-treated device had a rougher heterointerface morphology, which is in contrast to the negligibly different topography for the fresh films observed by AFM and SEM. This suggests that the roughening is inherent to the ageing process, possibly associated with heterointerface degradation by ion-migration-induced compositional loss. The elemental distributions were compared by X-ray energy-dispersive (EDX) mapping in STEM (Fig. 3c–f and Supplementary Fig. 11). On close inspection, large accumulations of both bromine (green arrows) and iodine (yellow arrows) can be seen for the OAI-treated device along the top Au/platinum (Pt) region. This is verified by quantitative analysis of

the elemental distributions (Fig. 3g–j). In consideration of the nominal stoichiometry of the perovskite, both bromine and iodine accumulation were approximately similar in order magnitude (Supplementary Fig. 12). We note that despite progress to completely remove the need for bromine in FAPbI<sub>3</sub>-based compositions<sup>17,18</sup>, it has been shown that bromine might remain necessary to stabilize the  $\alpha$ -FAPbI<sub>3</sub> phase in state-of-the-art devices<sup>19</sup>. The bulk devices that underwent FIB milling were further recovered and characterized by Bragg–Brentano XRD (Supplementary Fig. 13). The 8-FAPbI<sub>3</sub> peak supposedly at about 11.8° was not detected for both devices, and the  $\alpha$ -FAPbI<sub>3</sub> phase remained dominant, ruling out possible aggravation of the perovskite phase metastability by iodine interstitial generation<sup>20</sup>.

### Aggravated ion migration and device instability

We further simulated the ion migration pathways using the first-principles nudged-elastic-band methodology (Supplementary Note 6)<sup>12</sup>. To model the charge accumulation at the perovskite/spiro-MeOTAD heterointerface, we calculated the activation energy for halide migration in either a neutral uncharged or a negatively charged environment. Two independent pathways were explored: migration within a unit cell of a supercell (intra-lattice) and migration escaping a supercell (extra-lattice) (Extended Data Fig. 10 and Supplementary Table 5). The intra-lattice migration (vacancy mediated) investigates possible Coulombic screening effects by a charged environment to alter the bonding affinities and thus migration energetics<sup>21,22</sup>, whereas the extra-lattice migration is defect independent. For intra-lattice migration (Fig. 4a), the energy barriers for both iodine (~38.7%) and bromine (~29.4%) decreased substantially in the negatively charged environment. Similarly observed for the extra-lattice scenario (Fig. 4b), the activation energy for iodine

migration ( $-13.3\%$ ) and bromine migration ( $-17.8\%$ ) were both lower in the charged environment. Per the Arrhenius relationship, the rate constant has exponential dependence on the activation energy barrier.

Ion penetration can result in irreversible chemical reactions with spiro-MeOTAD to degrade its hole-transporting functionality<sup>23</sup>, and also chemical corrosion of the top electrode layer<sup>24</sup>, which potentially contributed to the  $V_{OC}$  and FF decays of the devices. The robust encapsulation procedure ruled out environmental degradation factors, indicating that intrinsic mechanisms (that is, ion migration) were responsible, and also excluded trapped charges catalysing extrinsic degradation pathways by moisture and oxygen<sup>25</sup>. This is evidenced by the short-circuit current retention for the devices, demonstrating the excellent phase stability of the active layers. By excluding ion migration, half-device tests further indicate that the photostability of the surface-treated films are negligibly different (Supplementary Note 7 and Supplementary Fig. 14). Tying together all results, we propose that the potential well and charge accumulation created by a negative  $\Delta E_{vac}$  aggravated device instability, by detrimentally accelerating halide migration at the spiro-MeOTAD/perovskite heterointerface. More generally, the beneficial improvements of surface treatments are sacrificially limited by a negative  $\Delta E_{vac}$ , but modulating the counteranion presents a simple method to further improve PSC stability and performance.

Backtracking, we also preliminarily explored the possible mechanistic origins of  $\Delta E_{vac}$  using first principles (full discussion in Supplementary Note 8), summarized as follows. Ligand-induced  $\Delta W$  originates from two independent contributions<sup>26,27</sup>: the ligand intrinsic dipole moment ( $\mu_{dipole}$ ), and a charge-density displacement by ligand–surface interactions and bond formation ( $\mu_{charge}$ ). The dipole moments of  $[OA]^+$  and  $[TsO]^-$  were  $+20.3\text{ D}$  and  $-10.5\text{ D}$ , respectively (Supplementary Figs. 15, 16). On the other hand,  $[TsO]^-$  induces a striking negative surface charge displacement,  $\bar{q}$ , of  $-0.022e$ , which is threefold larger in magnitude than the positive  $\bar{q}$  of  $[OA]^+$  ( $+0.006e$ ) (Fig. 4c–e and Supplementary Table 6). The negative  $\bar{q}$  sign of  $[TsO]^-$  indicates a depletion of electrons from the surface, and is equivalent to a positive  $\Delta W$ . This trend is reproducible even with defect states on the surface, or different surface concentrations and species (Supplementary Figs. 17, 18 and Supplementary Table 7). Therefore, we speculate that simultaneous contributions from both  $\mu_{charge}$  and  $\mu_{dipole}$  for  $[TsO]^-$  synergistically counterbalanced  $[OA]^+$ , to result in a net positive  $\Delta E_{vac}$  for the OATsO treatment. More broadly, this proposes design principles for the ideal perovskite/charge-transporting material heterointerface. We preliminarily tested pairing  $[TsO]^-$  with alkylammoniums with different chain lengths, but OATsO treatment yielded the best performance (Supplementary Fig. 19 and Supplementary Note 9).

## Online content

Any methods, additional references, Nature Research reporting summaries, source data, extended data, supplementary information, acknowledgements, peer review information; details of author contributions

and competing interests; and statements of data and code availability are available at <https://doi.org/10.1038/s41586-022-04604-5>.

- Lee, J.-W., Tan, S., Seok, S. I., Yang, Y. & Park, N.-G. Rethinking the A cation in halide perovskites. *Science* **375**, eabj1186 (2022).
- Jung, E. H. et al. Efficient, stable and scalable perovskite solar cells using poly(3-hexylthiophene). *Nature* **567**, 511–515 (2019).
- Jiang, Q. et al. Surface passivation of perovskite film for efficient solar cells. *Nat. Photon.* **13**, 460–466 (2019).
- Yoo, J. J. et al. An interface stabilized perovskite solar cell with high stabilized efficiency and low voltage loss. *Energy Environ. Sci.* **12**, 2192–2199 (2019).
- Ni, Z. et al. Resolving spatial and energetic distributions of trap states in metal halide perovskite solar cells. *Science* **367**, 1352–1358 (2020).
- Yang, Y. et al. Top and bottom surfaces limit carrier lifetime in lead iodide perovskite films. *Nat. Energy* **2**, 16207 (2017).
- Smith, M. B. & March, J. *March's Advanced Organic Chemistry: Reactions, Mechanisms, and Structure* 6th edn (Wiley, 2006).
- Bergmann, V. W. et al. Local time-dependent charging in a perovskite solar cell. *ACS Appl. Mater. Interfaces* **8**, 19402–19409 (2016).
- Cai, M. et al. Control of electrical potential distribution for high-performance perovskite solar cells. *Joule* **2**, 296–306 (2018).
- Söderström, T., Haug, F.-J., Terrazzoni-Daudrix, V. & Ballif, C. Optimization of amorphous silicon thin film solar cells for flexible photovoltaics. *J. Appl. Phys.* **103**, 114509 (2008).
- Tsai, H. et al. Design principles for electronic charge transport in solution-processed vertically stacked 2D perovskite quantum wells. *Nat. Commun.* **9**, 2130 (2018).
- Tan, S. et al. Steric impediment of ion migration contributes to improved operational stability of perovskite solar cells. *Adv. Mater.* **32**, 1906995 (2020).
- Azpiroz, J. M., Mosconi, E., Bisquert, J. & De Angelis, F. Defect migration in methylammonium lead iodide and its role in perovskite solar cell operation. *Energy Environ. Sci.* **8**, 2118–2127 (2015).
- Domanski, K. et al. Migration of cations induces reversible performance losses over day/night cycling in perovskite solar cells. *Energy Environ. Sci.* **10**, 604–613 (2017).
- Bai, S. et al. Planar perovskite solar cells with long-term stability using ionic liquid additives. *Nature* **571**, 245–250 (2019).
- Wang, Z. et al. Efficient ambient-air-stable solar cells with 2D–3D heterostructured butylammonium–caesium-formamidinium lead halide perovskites. *Nat. Energy* **2**, 17135 (2017).
- Kim, M. et al. Methylammonium chloride induces intermediate phase stabilization for efficient perovskite solar cells. *Joule* **3**, 2179–2192 (2019).
- Min, H. et al. Efficient, stable solar cells by using inherent bandgap of  $\alpha$ -phase formamidinium lead iodide. *Science* **366**, 749–753 (2019).
- Yoo, J. J. et al. Efficient perovskite solar cells via improved carrier management. *Nature* **590**, 587–593 (2021).
- Tan, S. et al. Shallow iodine defects accelerate the degradation of  $\alpha$ -phase formamidinium perovskite. *Joule* **4**, 2426–2442 (2020).
- Zhao, J. et al. Strained hybrid perovskite thin films and their impact on the intrinsic stability of perovskite solar cells. *Sci. Adv.* **3**, eaao5616 (2017).
- Lin, Y. et al. Excess charge-carrier induced instability of hybrid perovskites. *Nat. Commun.* **9**, 4981 (2018).
- Carrillo, J. et al. Ionic reactivity at contacts and aging of methylammonium lead triiodide perovskite solar cells. *Adv. Energy Mater.* **6**, 1502246 (2016).
- Besleaga, C. et al. Iodine migration and degradation of perovskite solar cells enhanced by metallic electrodes. *J. Phys. Chem. Lett.* **7**, 5168–5175 (2016).
- Ahn, N. et al. Trapped charge-driven degradation of perovskite solar cells. *Nat. Commun.* **7**, 13422 (2016).
- Heimel, G., Rissner, F. & Zojer, E. Modeling the electronic properties of  $\pi$ -conjugated self-assembled monolayers. *Adv. Mater.* **22**, 2494–2513 (2010).
- Brown, P. R. et al. Energy level modification in lead sulfide quantum dot thin films through ligand exchange. *ACS Nano* **8**, 5863–5872 (2014).
- Zerweck, U., Loppacher, C., Otto, T., Grafström, S. & Eng, L. M. Accuracy and resolution limits of Kelvin probe force microscopy. *Phys. Rev. B* **71**, 125424 (2005).

**Publisher's note** Springer Nature remains neutral with regard to jurisdictional claims in published maps and institutional affiliations.

© The Author(s), under exclusive licence to Springer Nature Limited 2022

## Methods

### Perovskite film fabrication

All materials were purchased from Sigma-Aldrich, unless otherwise stated. For the  $(\text{FAPbI}_3)_{0.95}(\text{MAPbBr}_3)_{0.05}$  composition, 889 mg ml<sup>-1</sup> FAPbI<sub>3</sub> (FAI, GreatCell Solar; PbI<sub>2</sub>, TCI America), 33 mg ml<sup>-1</sup> MAPbBr<sub>3</sub> (MABr, 1-Material; PbBr<sub>2</sub>, Alfa Aesar Chemicals) and 33 mg ml<sup>-1</sup> MACl (GreatCell Solar) were dissolved in a dimethylsulfoxide (DMSO)/dimethylformamide (DMF) mixed solvent (1:8 v/v). The films were deposited at 4,000 rpm for 20 s. After 10 s, 0.2 ml diethyl ether was dropped on the film. The film was then annealed for 10 min at 150 °C. For the FAPbI<sub>3</sub> composition, 1,266 mg FAPbI<sub>3</sub> and 34 mg MACl were dissolved in 192.8 µl N-methylpyrrolidone (NMP) and 1 ml DMF. The films were deposited at 4,000 rpm for 20 s. After 10 s, 0.2 ml diethyl ether was dropped on the film. The film was then annealed for 5 min at 100 °C, and subsequently 10 min at 150 °C. Subsequently, for post-fabrication surface treatment, 10 mM of the respective ammonium salts were dissolved in isopropyl alcohol, followed by deposition at 5,000 rpm for 30 s. Only OABr was dissolved in chloroform. All treatments, except with phenethylammonium iodide (PEAI), were annealed at 100 °C for 5 min. No annealing was done for PEAI. The reference films without post-treatment were washed with pure isopropyl alcohol at 5,000 rpm, followed by 100 °C annealing for 5 min.

### Device fabrication

Substrates of ITO on glass were cleaned by successive ultrasonication in detergent, deionized water, acetone and isopropyl alcohol, for 20 min each. Cleaned substrates were treated by ultraviolet ozone for 20 min. For the electron-transporting material, SnO<sub>2</sub> colloidal solution (Alfa Aesar Chemicals) was diluted in water in a 1:5 ratio. The solution was spun at 3,000 rpm for 30 s, and the film was subsequently annealed for 35 min at 165 °C. Ten-millimolar potassium hydroxide or potassium chloride in water was spun at 3,000 rpm for 30 s, and subsequently annealed at 100 °C for 10 min. We note that potassium chloride treatment was slightly improved over potassium hydroxide. The perovskite film fabrication and post-treatment procedures were performed as described above. Subsequently, 60.0 mg spiro-MeOTAD (p-OLED), 25.5 µl 4-tert-butylpyridine, 15.5 µl bis(trifluoromethane)sulfonimide lithium salt (520 mg ml<sup>-1</sup> in acetonitrile) and 12.5 µl of FK209 (p-OLED; 375 mg ml<sup>-1</sup> in acetonitrile) were dissolved in 0.7 ml chlorobenzene. The solution was spun at 3,000 rpm for 30 s. For the top electrode, 100-nm gold was thermally deposited at an evaporation rate of 0.5 Å s<sup>-1</sup>. The device active area is determined by a shadow mask to be 0.13 cm<sup>2</sup>. For the anti-reflection coating, 150-nm magnesium fluoride (MgF<sub>2</sub>) was thermally deposited at an evaporation rate of 1 Å s<sup>-1</sup>. MgF<sub>2</sub> was deposited on all devices, unless otherwise stated.

### AFM and KPFM

To obtain the spatial variation of the work function for each perovskite sample, we performed KPFM, which is an AFM-based technique to acquire work function information of the sample surface via measuring the contact potential difference for every pixel. For cross-sectional KPFM, the devices were cleaved simply to expose their cross-sections. A map of contact potential difference, or the relative surface potential of a sample to that of a biased AFM tip, is simultaneously obtained with a topographic image of the sample surface. The work function of the AFM tip is calibrated before and after every measurement with highly ordered pyrolytic graphite, whose work function is well known to be 4.6 eV. The real work function value of each perovskite sample is calculated from the measured surface potential of each sample, with respect to the tip work function. The temperature and humidity near the AFM were recorded before every measurement.

The AFM tips used for the KPFM measurement are Au-coated NSC36/chromium–Au tips (MikroMasch) as the measurement of electric properties requires at least one conductive component. Also, each KPFM

measurement involved the electrically grounded perovskite samples with conductive sample holders, through which the surface potential of any sample may have the same zero point. All AFM-based measurements were conducted with a commercial AFM NX-10 (Park Systems).

### STEM and EDX

The STEM images and EDX maps were taken using a JEOL 2800 S/TEM equipped with dual 100-mm<sup>2</sup> silicon drift detectors at 200 kV with a probe size of 1 nm. To perform the STEM analyses on the devices, the device cross-section was lifted out and mounted on a copper (Cu) grid using a Tescan GAIA3 SEM/FIB microscope. The sample was protected by a 2-µm-thick Pt layer to prevent gallium implantation during the milling procedure. The sample was successively polished, first using 30 kV and 600 pA, then subsequently at 15 kV and 150 pA, and finally at 3 kV and 90 pA, until reaching electron-transparent thickness.

### First-principles density functional theory computation

All bulk and slab first-principles calculations were performed using density functional theory (DFT) in the plane-wave/pseudopotential approach implemented in the Vienna Ab initio Simulation (VASP) package<sup>29</sup>. A revised Perdew–Burke–Ernzerhof generalized gradient approximation (PBEsol) was used for the exchange-correlation functional<sup>30</sup>. We included dispersion corrections to the total energy using Grimme's DFT-D3 scheme<sup>31</sup>. Projector-augmented-wave (PAW) pseudopotentials were used to describe valence–core interactions<sup>32</sup>. Plane-wave expansions with kinetic energies up to 300 eV were chosen. Both ionic positions and supercell dimensions were allowed to relax using conjugate gradient algorithm until all residual forces were smaller than 0.02 eV·Å<sup>-1</sup>. Bulk 4 × 4 × 4 and slab 4 × 4 × 1 Γ-centre *k*-point meshes were adopted for Brillouin-zone sampling. For bulk calculations, 2 × 2 × 2 supercells were used. For surface-energy calculations, the 2 × 2 × *L* surfaces (*L* is the number of perovskite layers in the slab) were formed along (001) by periodic slabs including 9 to 11 atomic layers for a surface separated by 10–15 Å of vacuum.

For the electrostatic potential maps, all structures were pre-optimized with the very tight GFN2-xTB method using the xTB program (version 6.2)<sup>33,34</sup> before conformational search. Conformational analysis of each structure was performed in water using metadynamic sampling in the extended tight binding Conformer–Rotamer Ensemble Sampling Tool (xtb CREST) program package (version 6.2)<sup>35</sup>. The iMTD–GC workflow was used for the conformational search algorithm with 6 kcal mol<sup>-1</sup> energy and 0.5-Å root mean square deviation thresholds at 298.15 K.

All further DFT calculations of the lowest conformers were performed using Gaussian16. Geometry optimization and frequency calculations were completed at the ωB97X-D/6-311++G(d,p) level in the gas phase. Optimized structures were verified by frequency calculations as minima (zero imaginary frequencies). Electrostatic potential charges and maps were computed with the B3LYP method, the GD3BJ<sup>36</sup> empirical dispersion and the LANL2DZ basis set for iodide, and the aug-cc-pvtz basis set for all other atoms based on the Hirshfeld population analysis<sup>37</sup>. Dipoles were calculated with the ωB97X-D/6-31+G(d) method and basis set. Electrostatic potential maps were generated using GaussView 6.0.16.

### Preparation of ammonium salts

p-Toluenesulfonic acid monohydrate was first dehydrated to remove the water of crystallization. Using 100 ml toluene dissolves 1 g p-toluenesulfonic acid monohydrate in a 250-ml two-neck round-bottom flask. Vacuum distillation of toluene (about 20 mm Hg is a sufficient vacuum to lower the boiling point of toluene to a reasonable value) was followed to obtain solid p-toluenesulfonic acid using a vacuum oven at 100 °C for 1 week. For the anion substitution of alkylammonium salts, alkylamine (for example, octylamine) was added stoichiometrically to the acid (for example, p-toluenesulfonic acid) in an isopropyl alcohol mixed solvent, followed by stirring at 50 °C overnight. The chemical structure and purity of the salt was further

verified by  $^1\text{H}$  NMR (Supplementary Note 10, Supplementary Fig. 20). Typically, a concentrated stock solution ( $>500$  mM) is first prepared, followed by solution dilution to reach the final 10-mM concentration. Trifluoroacetic acid ( $>99.5\%$ ) was obtained from EMD Millipore. Octylammonium iodide and octylammonium bromide were purchased commercially from GreatCell Solar.

### Device encapsulation and stability testing

Device encapsulation was carried out inside a nitrogen-filled glovebox ( $<0.6$  ppm of  $\text{O}_2/\text{H}_2\text{O}$ ) by using an ultraviolet-curable adhesive (Nagase America) applied to a custom-designed cover glass (AMG Korea). The glovebox was completely absent of any chemical solvents to ensure a pristine atmosphere. The devices were kept in the glovebox for at least 2 h before and after encapsulation. The cover glass was superimposed on the active layer and fixed in position with the adhesive. This was then exposed to ultraviolet illumination for 2 min to cure the adhesive and seal the cover glass to the device. Care was taken to block the device active-layer area from the ultraviolet illumination by superimposing black electrical tape on the cover glass area that corresponded to the device active-layer area. We note that in our experience, it was important to pay attention to the expiry date of the ultraviolet-curable adhesive, with fresh adhesives preferred.

For the MPP stability testing, encapsulated devices were exposed to continuous illumination by a simulated air mass 1.5G spectrum illumination from a solar simulator. The devices were biased with a voltage corresponding to their MPP. The aging atmosphere was open ambient air (relative humidity (RH)  $40 \pm 10\%$ ). For the OC stability testing, encapsulated devices were exposed to continuous illumination by a metal halogen lamp source ( $90 \pm 10$  mW cm $^{-2}$ ). The devices were placed in an in-house-built aging chamber under the OC condition. The chamber atmosphere was open ambient air (RH  $40 \pm 10\%$ ). Periodically, the devices were transferred to a simulated AM 1.5G spectrum illumination from a solar simulator, also in ambient air (RH  $40 \pm 10\%$ ), to measure their performance. The devices were immediately returned to the aging chamber upon measurement completion.

### Material and device characterization

SEM was carried out using an FEI Nova NanoLab 600 DualBeam (FIB/SEM) instrument in secondary electron mode. The films were coated with an approximately 1-nm-thick Au layer by sputtering to prevent charging during the measurement. XPS measurements were carried out on an XPS AXIS Ultra DLD (Kratos Analytical). An Al K $\alpha$  (1,486.6 eV) X-ray was used as the excitation source. UPS measurements were carried out using a helium discharge lamp, emitting ultraviolet energy at 21.2 eV. All UPS measurements were performed using standard procedures with a  $-9$ -V bias applied between the samples and the detectors. PL spectroscopy was performed with a Horiba Jobin Yvon system, with a 532-nm xenon lamp or a 640-nm monochromatic laser excitation source. Time-resolved PL spectra were measured using a PicoHarp 300 with time-correlated single-photon counting capabilities (PLD 800B, PicoQuant) with a repetition frequency of 100 kHz. The confocal PL maps were measured using a Leica Confocal SP8-STED/FLIM/FCS confocal laser scanning microscope, using an HC PL APO oil objective ( $40\times/1.40$ ) and a 514-nm argon pulsed diode laser. XRD was performed by an X-ray PANalytical diffractometer at a scan rate of  $4^\circ \text{ min}^{-1}$  with a Cu K $\alpha$  radiation source. The simulated AM 1.5G 1-sun spectrum illumination ( $100$  mW cm $^{-2}$ ) was from an Oriel Sol3A class AAA solar simulator (Newport). The light intensity was first calibrated with an National Renewable Energy Laboratory (NREL)-certified silicon photodiode with a KG-5 filter. A Keithley 2401 source meter was used to perform the current density–voltage device measurements. A  $0.100\text{-cm}^2$ -sized metal aperture was used to precisely define the device active area during measurement. The external quantum efficiency (EQE) was measured with a custom-designed Enlitech system under a.c. mode (frequency 133 Hz) without light bias with a lock-in amplifier

with a current preamplifier under a short-circuit condition. The phototransient measurements were done with a pulsed red dye laser (Rhodamine 6G, 590 nm) pumped by a nitrogen laser (LSI VSL-337ND-S) as the perturbation source. The pulse width was 4 ns at a repetition frequency of 10 Hz. The laser pulse intensity was monitored to maintain the amplitude of transient  $V_{oc}$  below 5 mV. Then, the voltage under the OC condition and the current under the short-circuit condition were measured over a  $1\text{-M}\Omega$  resistor and a  $50\text{-}\Omega$  resistor, and recorded on a digital S4 oscilloscope (Tektronix DPO 4104B).

### Data availability

The data that support the findings of this study are available from the corresponding authors on reasonable request.

29. Kresse, G. & Furthmüller, J. Efficiency of ab-initio total energy calculations for metals and semiconductors using a plane-wave basis set. *Comput. Mater. Sci.* **6**, 15–50 (1996).
30. Perdew, J. P. et al. Restoring the density-gradient expansion for exchange in solids and surfaces. *Phys. Rev. Lett.* **100**, 1–4 (2008).
31. Grimme, S., Antony, J., Ehrlich, S. & Krieg, H. A consistent and accurate ab initio parametrization of density functional dispersion correction (DFT-D) for the 94 elements H–Pu. *J. Chem. Phys.* **132**, 154104 (2010).
32. Blöchl, P. E. Projector augmented-wave method. *Phys. Rev. B* **50**, 17953–17979 (1994).
33. Grimme, S., Bannwarth, C. & Shushkov, P. A robust and accurate tight-binding quantum chemical method for structures, vibrational frequencies, and noncovalent interactions of large molecular systems parametrized for all *spd*-block elements ( $Z = 1$ –86). *J. Chem. Theory Comput.* **13**, 1989–2009 (2017).
34. Bannwarth, C., Ehlert, S. & Grimme, S. GFN2-xTB—an accurate and broadly parametrized self-consistent tight-binding quantum chemical method with multipole electrostatics and density-dependent dispersion contributions. *J. Chem. Theory Comput.* **15**, 1652–1671 (2019).
35. Grimme, S. et al. Fully automated quantum-chemistry-based computation of spin–spin-coupled nuclear magnetic resonance spectra. *Angew. Chem. Int. Edn* **56**, 14763–14769 (2017).
36. Grimme, S., Ehrlich, S. & Goerigk, L. Effect of the damping function in dispersion corrected density functional theory. *J. Comput. Chem.* **32**, 1456–1465 (2011).
37. Hirshfeld, F. L. Bonded-atom fragments for describing molecular charge densities. *Theor. Chim. Acta* **44**, 129–138 (1977).

**Acknowledgements** This work was supported by the US Department of Energy’s Office of Energy Efficiency and Renewable Energy (EERE) under the Solar Energy Technologies Office under award number DE-EE0008751. J.-W.L. acknowledges support from a Korea Institute of Energy Technology Evaluation and Planning (KETEP) grant funded by the Korea government (MOTIE) (grant numbers 2021400000640, 20213030010400) and a POSCO Science Fellowship from the POSCO TJ Park Foundation. The TEM work at UC Irvine was supported by the National Science Foundation (NSF) under grant number DMR-2034738. Part of the computing resources used in this work were provided by the National Center for High-Performance Computing of Turkey (UHEM). Y.J.S. and J.-W.L. acknowledge support by the National Research Foundation of Korea (NRF) grant funded by the Korea government (MSIT) (grant numbers NRF-2022R1C1C1011975 and NRF-2021R1A2C2007141). N.-G.P. acknowledges financial support from NRF grants funded by MSIT under contract NRF-2021R1A3B1076723 (Research Leader Program). We acknowledge the use of facilities and instrumentation at the UC Irvine Materials Research Institute (IMRI), which is supported in part by the National Science Foundation through the UC Irvine Materials Research Science and Engineering Center (DMR-201967). Work at the Molecular Foundry was supported by the Office of Science, Office of Basic Energy Sciences, of the US Department of Energy under contract number DE-AC02-05CH11231. We thank M. E. Liao, K. Huynh, M. S. Goorsky, S. Nuryyeva, K. N. Houk, K.-H. Wei and B. Jeong for experimental assistance, measurements or discussions; and S. Shelton, Y. Liu and the Molecular Foundry for the third-party laboratory device efficiency measurements.

**Author contributions** S.T., T.H. and Y.Y. conceived the idea. S.T. and T.H. designed and conducted most of the experiments, supervised by Y.Y., T.W.Y., K.P., D.-K.L. and T.Y. performed the KPFM and AFM measurements and analysed the data, supervised by Y.J.S., J.-W.L. and N.-G.P. I.Y. did the theoretical calculations, modelling and data analysis. M.X. performed the STEM and EDX measurements and analysis, supervised by X.P.Q.X. performed the confocal PL mapping and part of the UPS measurements. C.-H.C., R.Z. and D.M. performed the chemical synthesis. Q.X. and K.P. assisted with experiments and film and device fabrication. R.W., Y.Z., H.-C.W., J.X. and J.-W.L. assisted with data analysis and discussion. S.T., T.H., R.W., J.-W.L. and Y.Y. wrote the manuscript, and all authors contributed feedback and commented on the manuscript.

**Competing interests** The authors declare no competing interests.

### Additional information

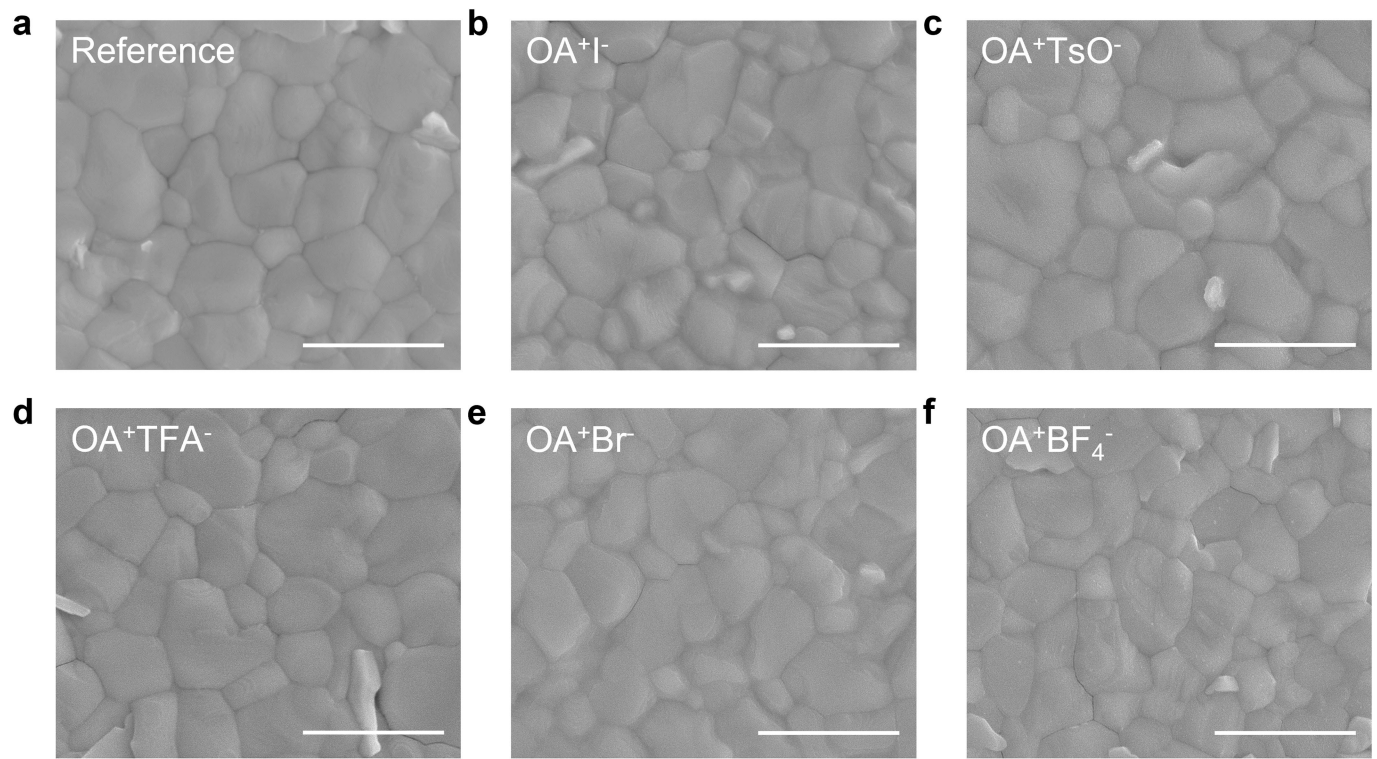
**Supplementary information** The online version contains supplementary material available at <https://doi.org/10.1038/s41586-022-04604-5>.

**Correspondence and requests for materials** should be addressed to Rui Wang, Jin-Wook Lee or Yang Yang.

**Peer review information** *Nature* thanks the anonymous reviewer(s) for their contribution to the peer review of this work.

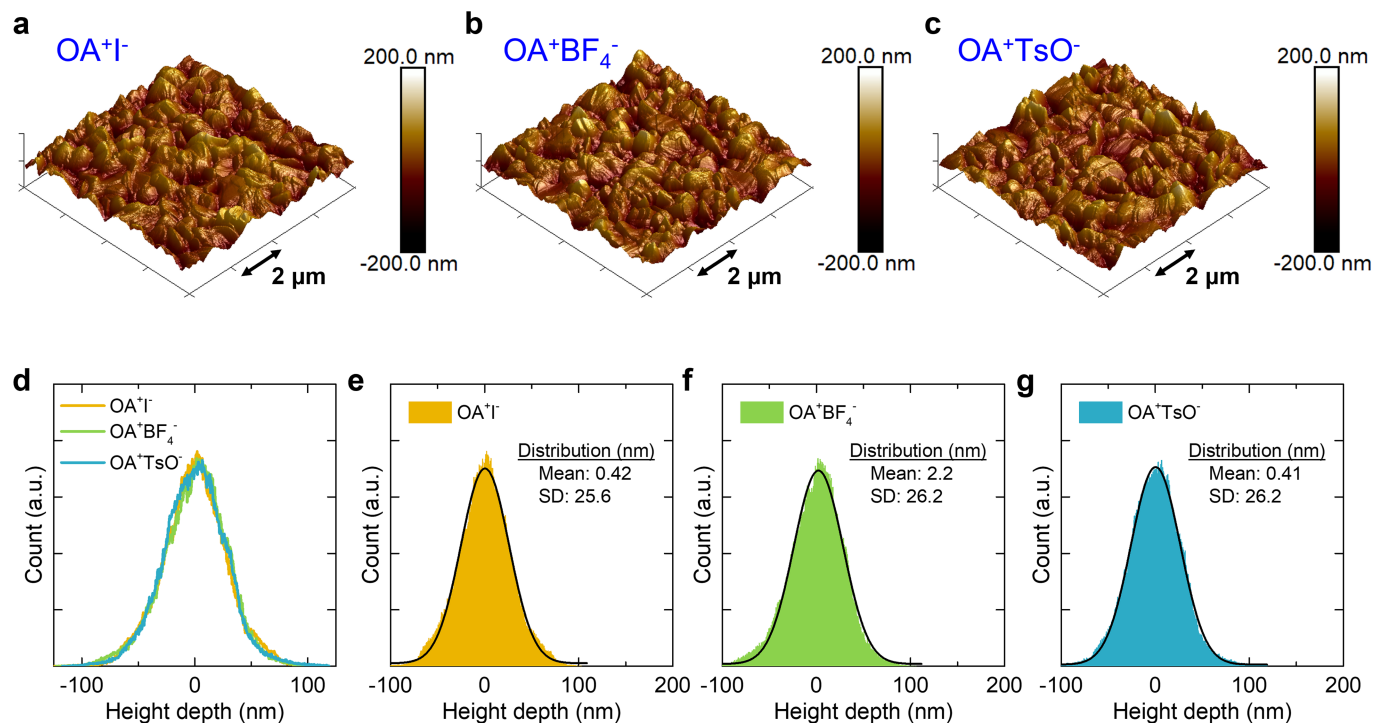
**Reprints and permissions information** is available at <http://www.nature.com/reprints>.

# Article



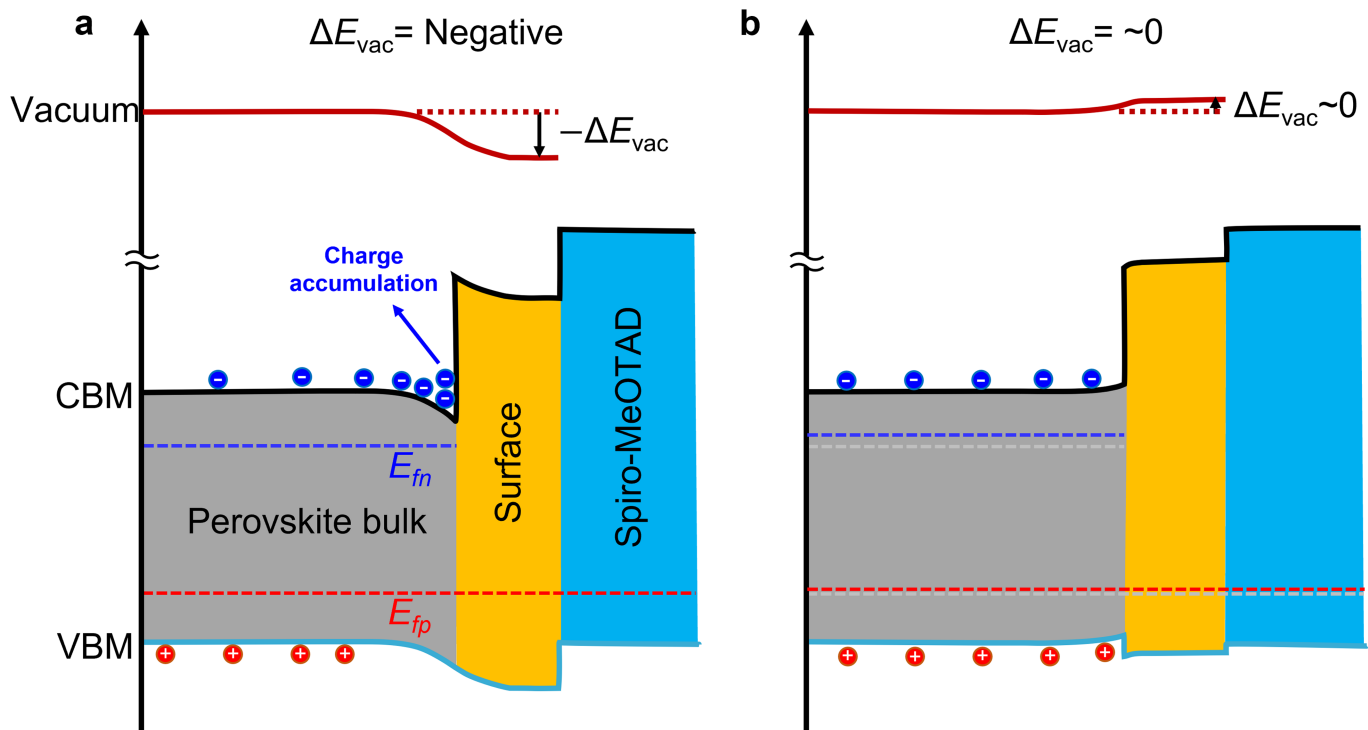
**Extended Data Fig. 1 | Morphology of the perovskite films.** Surface morphology of the: **a**, reference; **b**, OAI-treated; **c**, OATsO-treated; **d**, OATFA-treated; **e**, OABr-treated; and **f**, OABF<sub>4</sub>-treated perovskite films measured by

SEM. All scale bars represent 2  $\mu$ m. No obvious difference can be seen between the reference and treated perovskite films.



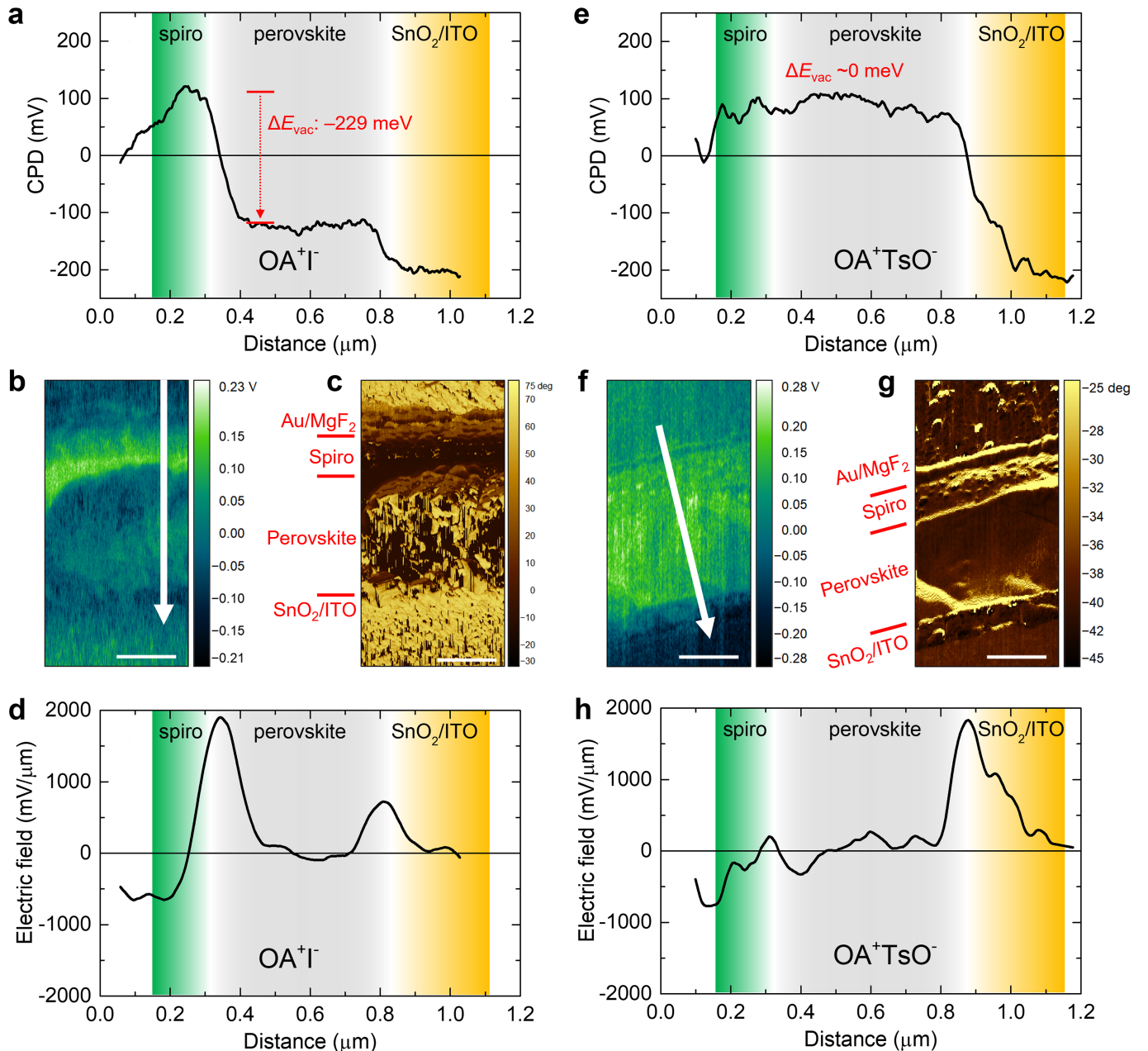
**Extended Data Fig. 2 | Topography of the passivated perovskite films.**  
Representative 3D topography of the: **a**, OAI-treated; **b**, OABF<sub>4</sub>-treated; and **c**, OATsO-treated perovskite films measured by AFM. All scale bars represent 2 μm. **d**, Comparison of the height depth distribution of the films. Depth

distribution histograms for the: **e**, OAI-treated; **f**, OABF<sub>4</sub>-treated; and **g**, OATsO-treated perovskite films. Insets include the fitted statistical parameters. SD, standard deviation.



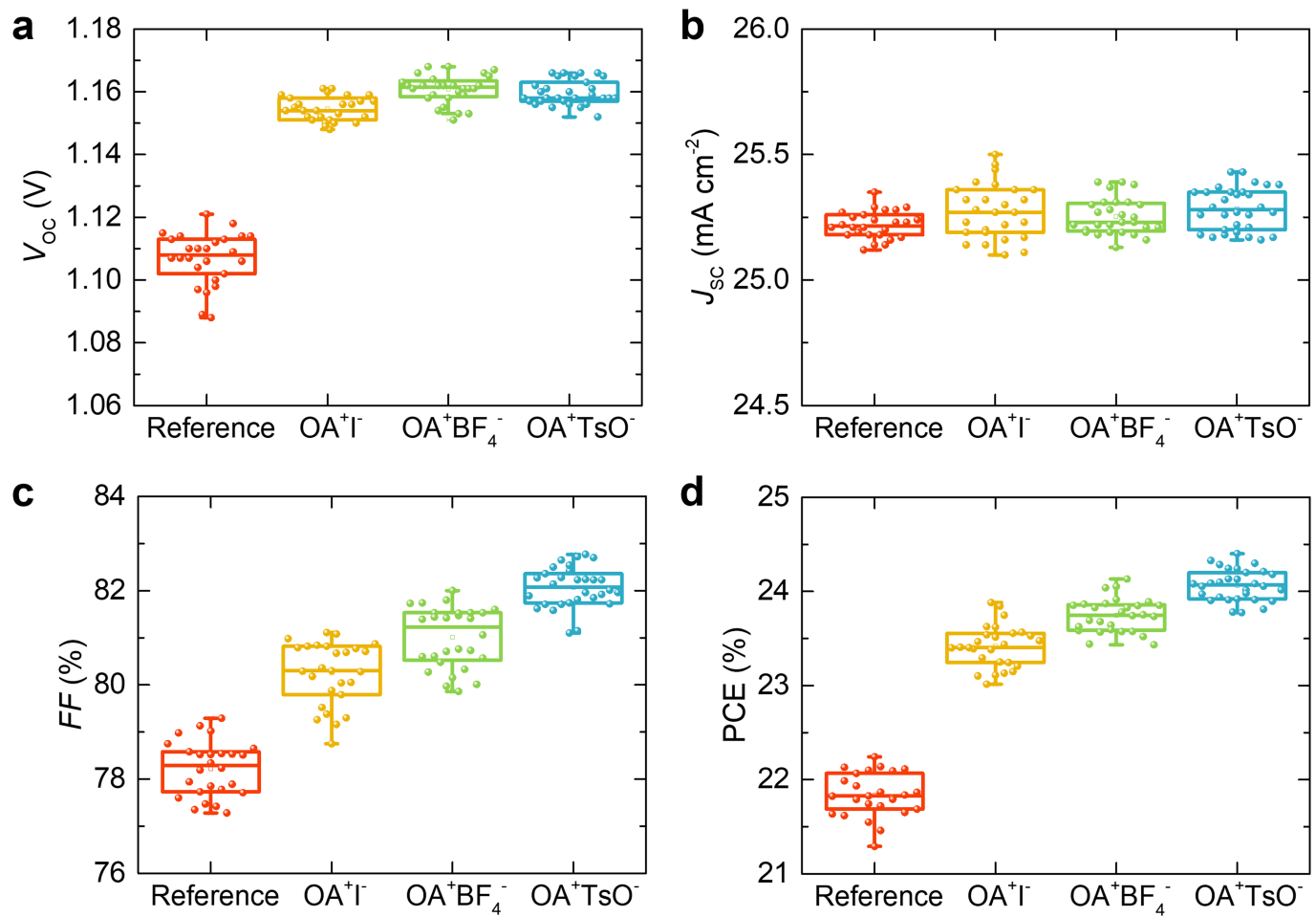
**Extended Data Fig. 3 | Heterointerface energy band diagrams.** Schematic interpretation of the heterointerface band alignments of the **a**, OAI-treated and **b**, OATsO-treated devices under illumination in open-circuit condition. The band alignments are constructed based on the UPS and KPFM results. CBM, conduction band minimum; VBM, valence band maximum;  $E_{fn}$ , electron

quasi-fermi level;  $E_{fp}$ , hole quasi-fermi level. The dashed gray lines in **b** indicate  $E_{fn}$  and  $E_{fp}$  of the OAI-treated device from **a**. The diagrams are not drawn to scale. Both surface treatments create a type I energy alignment at the heterointerface, but the vacuum level upshift of the OATsO-treated device minimized the potential well to mitigate the electron accumulation.

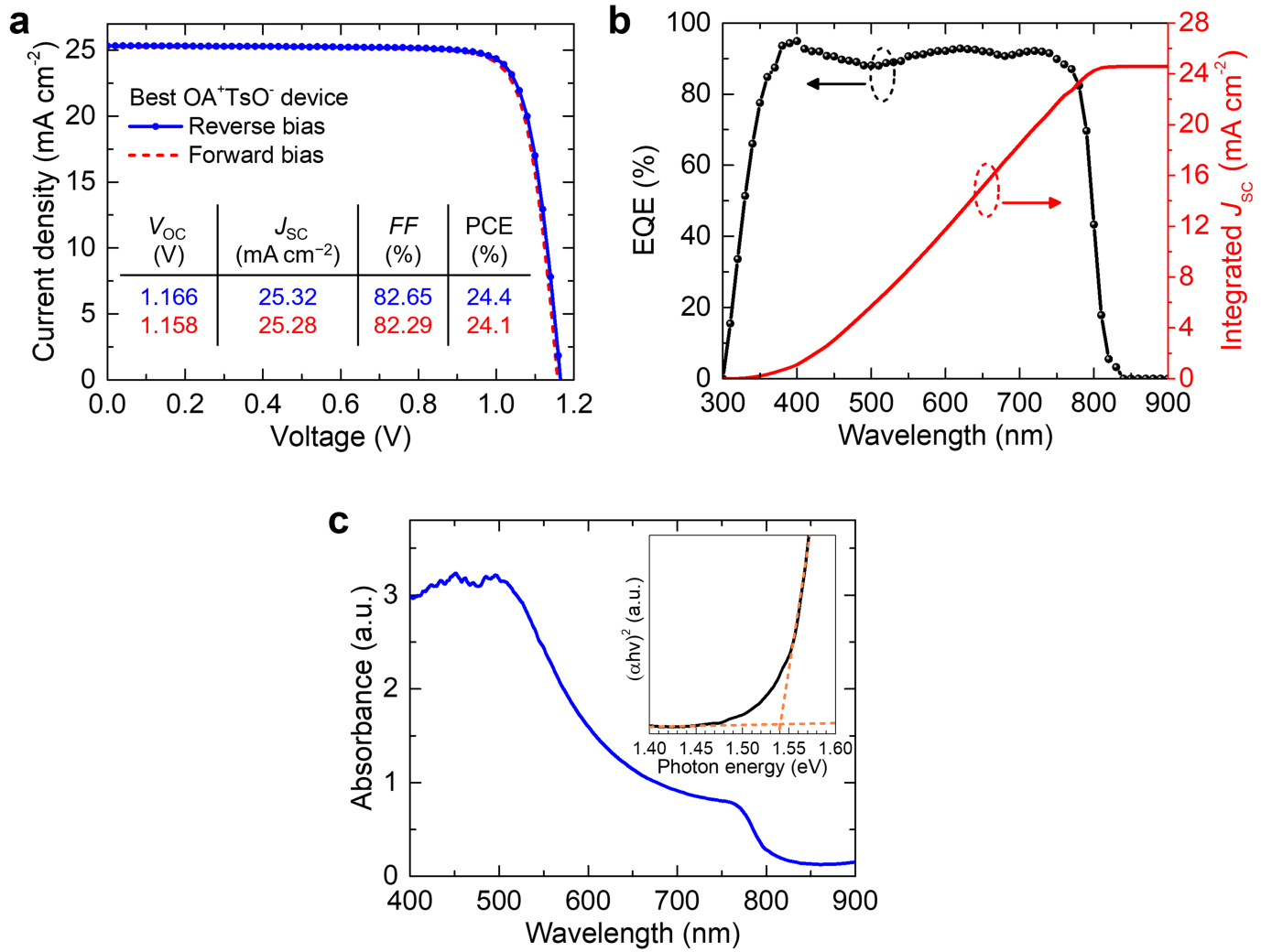


**Extended Data Fig. 4 | Device cross-sectional KPFM profiling.** **a**, CPD profile; **b**, KPFM spatial mapping; **c**, corresponding AFM spatial mapping; and **d**, electric field distribution of the OA<sup>+</sup>I<sup>-</sup>-treated device. **e**, CPD profile; **f**, KPFM spatial mapping; **g**, corresponding AFM spatial mapping; and **h**, electric field distribution of the OA<sup>+</sup>TsO<sup>-</sup>-treated device. Measurements were performed under illumination in open-circuit condition. All scale bars represent 300 nm. The CPD offsets were adjusted such that the CPD value of the buffer layer

becomes zero. Note that this does not affect the electric field and charge displacement profiles, which calculate the derivatives of the CPD profiles. Although we do not expect the rough morphology seen in **c** to affect the KPFM signal, we cannot completely rule this out at this stage. Therefore, we have repeated the KPFM measurement on another separate OA<sup>+</sup>I<sup>-</sup>-treated device. As shown in Supplementary Fig. 4, we were able to reproduce the potential drop at the perovskite/spiro-MeOTAD heterointerface.



**Extended Data Fig. 5 | Device photovoltaic parameters.** Box plots showing the distribution of the: **a**,  $V_{OC}$ ; **b**,  $J_{SC}$ ; **c**, FF; and **d**, PCE of the devices. Centre line, median; box limits, 25<sup>th</sup> and 75<sup>th</sup> percentiles; whiskers, outliers.

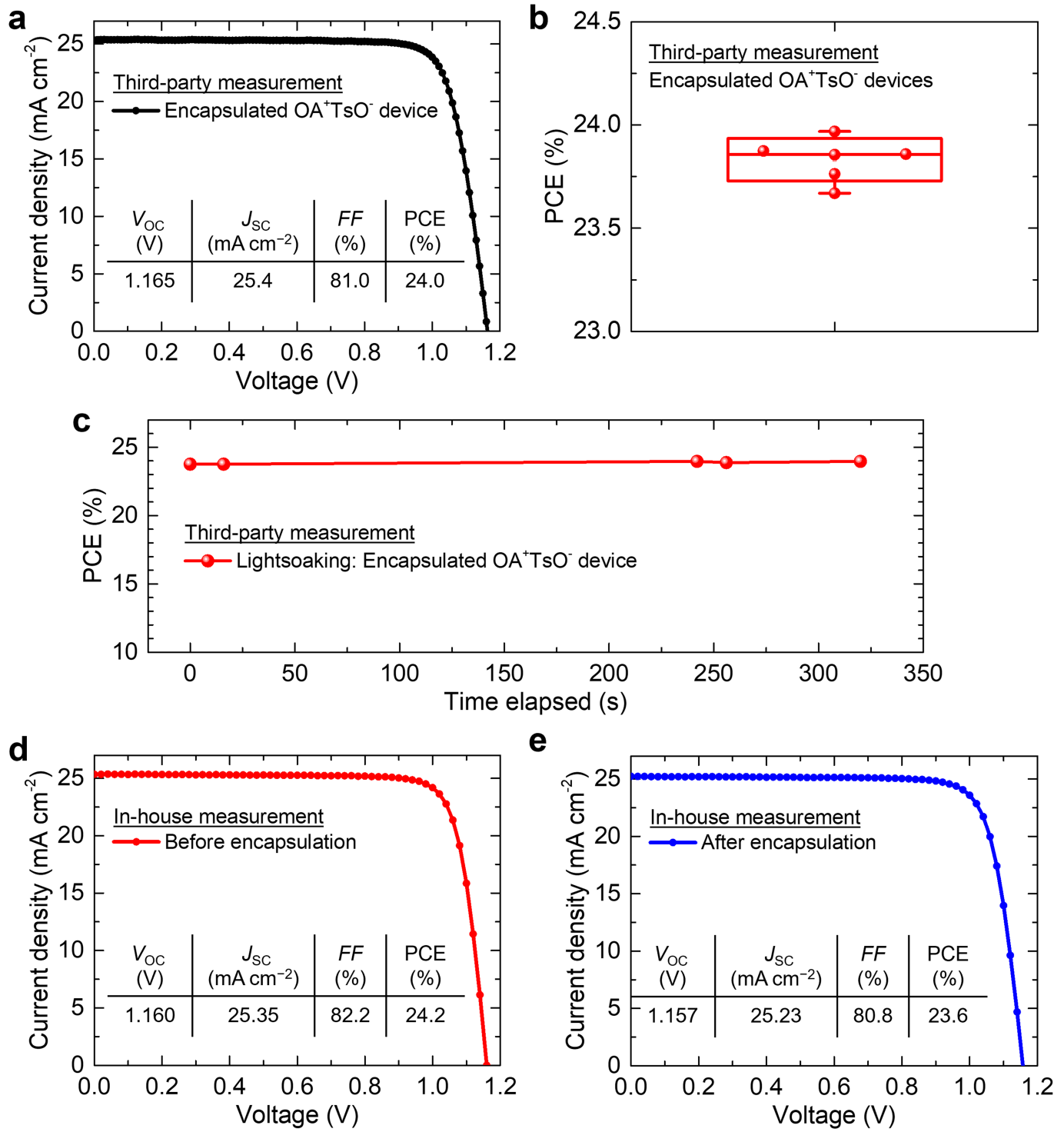


**Extended Data Fig. 6 | Characterization of the OATsO-treated devices.**

**a**, Current density-voltage curves of the best-performing OATsO-treated device, in reverse scan (blue line) and forward scan (red line). Inset includes the measured photovoltaic parameters. **b**, EQE spectrum and integrated  $J_{SC}$  of an OATsO-treated device. The integrated  $J_{SC}$  is  $24.6 \text{ mA cm}^{-2}$ , and therefore

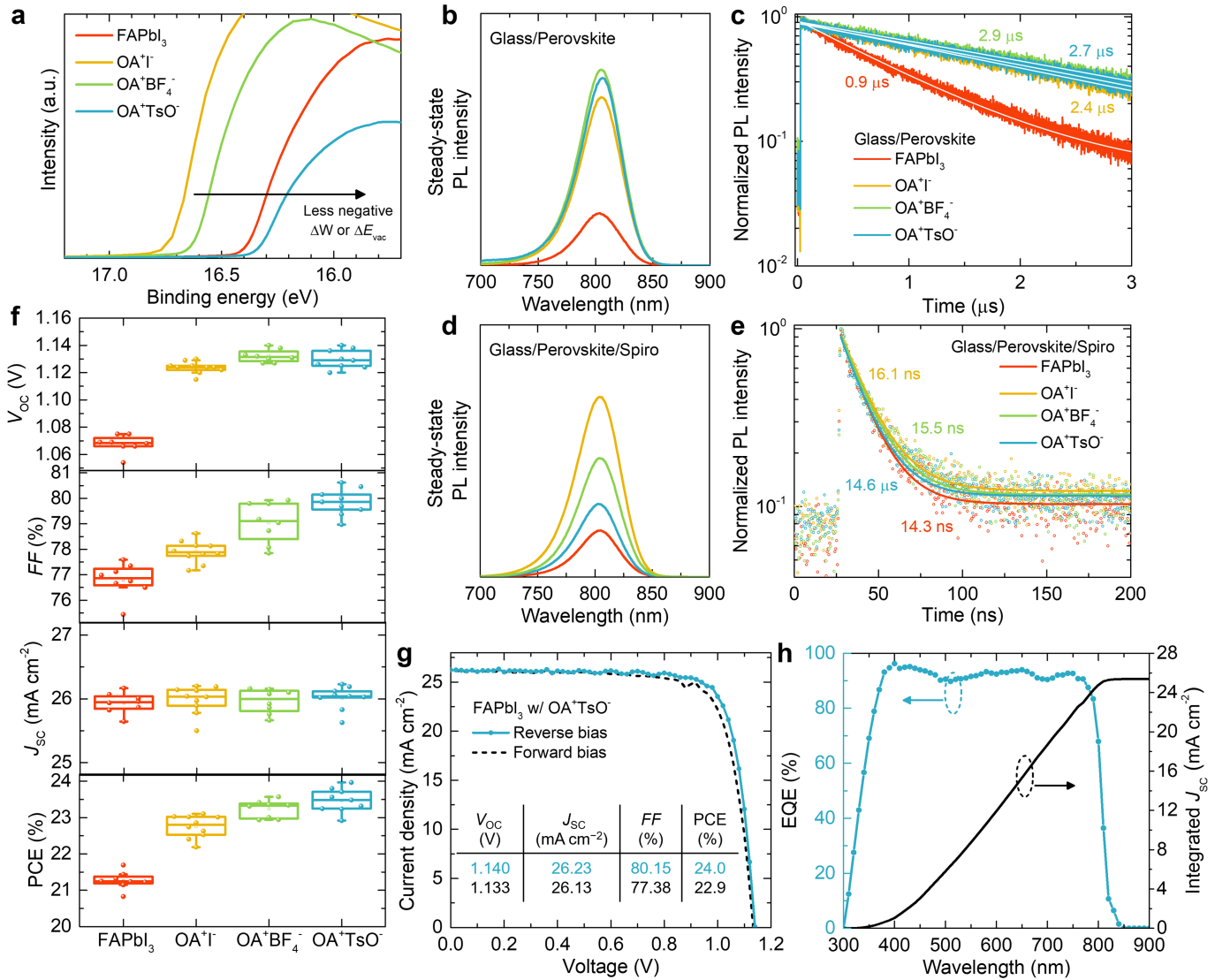
well matched (less than 3% discrepancy) with the measured value.

**c**, Absorbance profile of an OATsO-treated film on glass measured by UV-Vis spectroscopy. Inset includes a Tauc plot and linear fits to estimate the optical bandgap.



**Extended Data Fig. 7 | Third-party device performance measurements.** **a**, Current density–voltage curve, and **b**, box plot showing the PCE distribution of the encapsulated OATsO-treated devices. Measurements were performed at the Molecular Foundry, Berkeley, CA, USA. As the measurements were fully done in ambient air (RH approximately 50%), all devices had to be

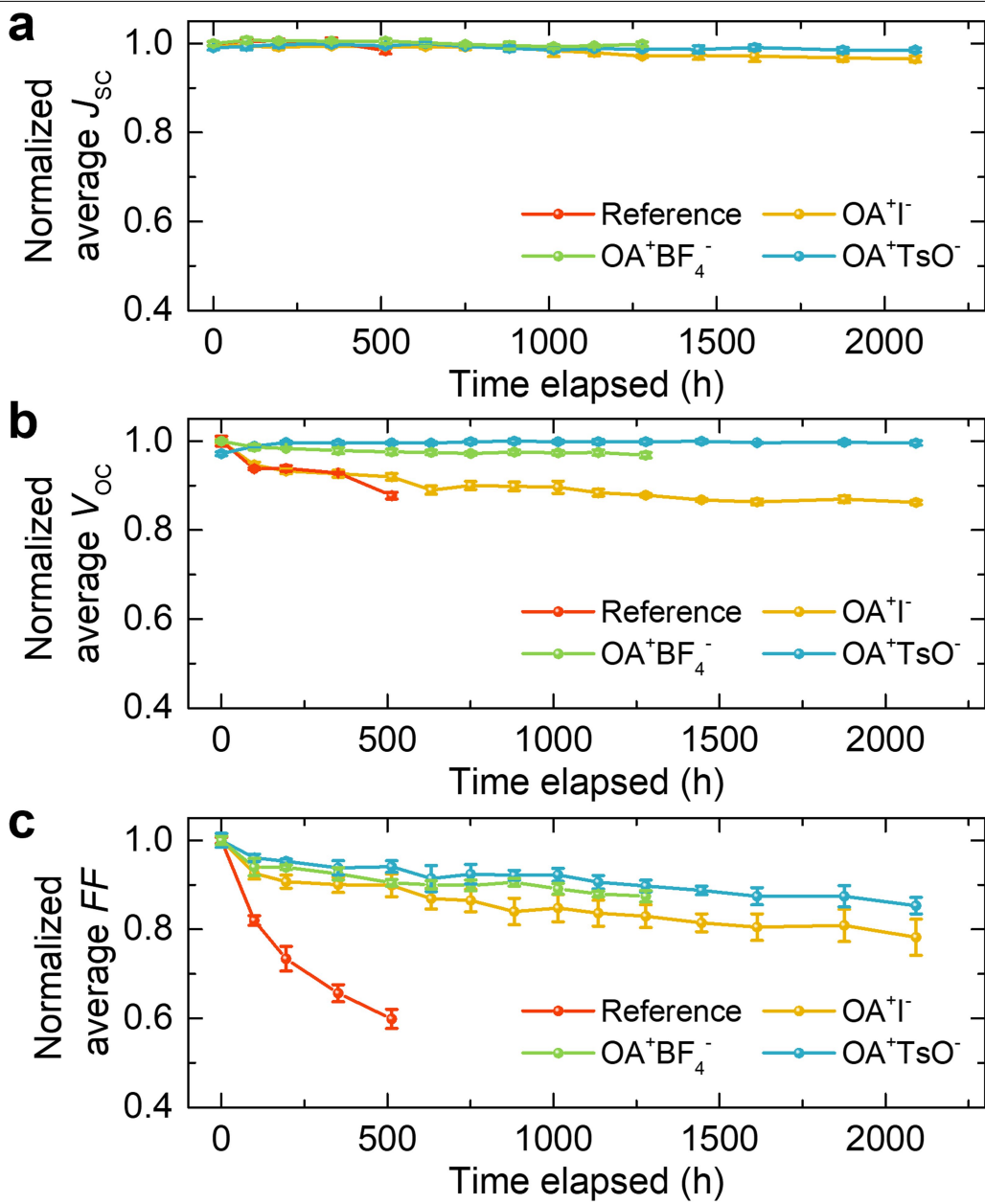
encapsulated, which resulted in a drop in performance. **c**, PCE evolution with time under lightsoaking of an encapsulated OATsO-treated device. Current density–voltage curves of the same device **d**, before and **e**, after the encapsulation procedure, measured in-house.



#### Extended Data Fig. 8 | Universality verification on a FAPbI<sub>3</sub> composition.

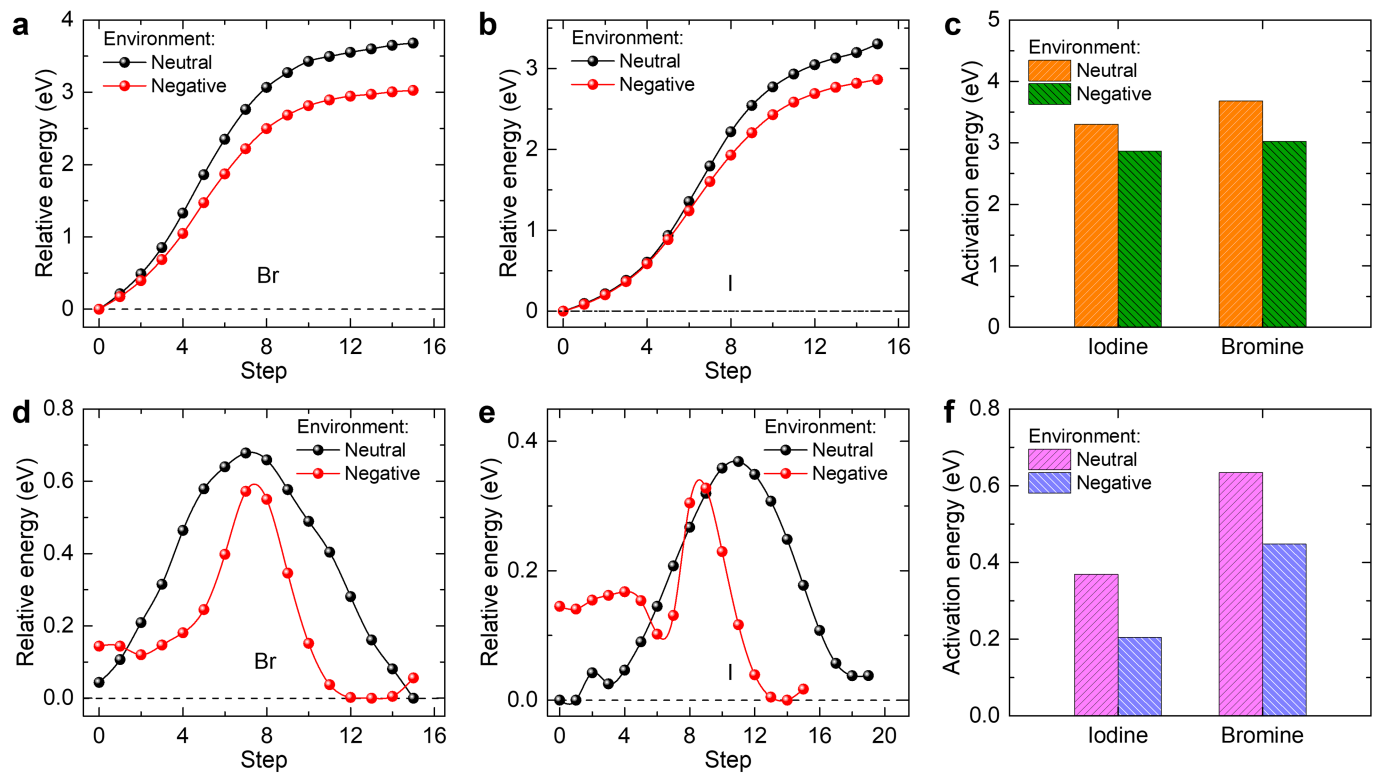
**a**, UPS secondary electron cut-offs of the perovskite films. **b**, Steady-state and **c**, time-resolved PL spectra of the glass/perovskite films. **d**, Steady-state and **e**, time-resolved PL spectra of the glass/perovskite/spiro-MeOTAD films. The carrier lifetimes are fitted with a mono-exponential decay function. **f**, Box plots

of the distribution of the device photovoltaic parameters. Centre line, median; box limits, 25<sup>th</sup> and 75<sup>th</sup> percentiles; whiskers, outliers. **g**, Current density-voltage curves and **h**, EQE spectrum and integrated  $J_{\text{SC}}$  of the best-performing device treated with OA+TsO-. The integrated  $J_{\text{SC}}$  is 25.4  $\text{mA cm}^{-2}$ , well matched (approximately 3% discrepancy) with the measured scan value.

**Extended Data Fig. 9 | Open-circuit stability test device performance.**

Evolution with time of the normalized average **a**,  $J_{sc}$ , **b**,  $V_{oc}$ , and **c**, FF of the devices under continuous illumination with a metal halogen lamp. The

encapsulated devices were aged in ambient atmosphere at RH - 40% and T - 40 °C in open-circuit condition. Error bars represent the standard deviation of four devices for each condition.



**Extended Data Fig. 10 | Activation energy for halide migration.** **a–c**, Energy profiles for the extra-lattice migration of **a**, bromine and **b**, iodine in a neutral uncharged or negatively charged environment, and **c**, corresponding

activation energy barriers. **d–f**, Energy profiles for the intra-lattice migration of **d**, bromine and **e**, iodine in a neutral uncharged or negatively charged environment, and **f**, corresponding activation energy barriers.